Page Proof Instructions and Queries

Journal Title: Journal of Mechanical Engineering Science, Proceedings of the Institution of Mechanical Engineers Part C [PIC]

Article Number: 705906

Thank you for choosing to publish with us. This is your final opportunity to ensure your article will be accurate at publication. Please review your proof carefully and respond to the queries using the circled tools in the image below, which are available **by clicking "Comment"** from the right-side menu in Adobe Reader DC.*

Please use *only* the tools circled in the image, as edits via other tools/methods can be lost during file conversion. For comments, questions, or formatting requests, please use T. Please do *not* use comment bubbles/sticky notes.

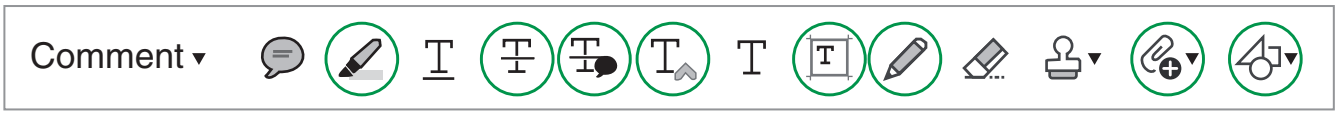

*If you do not see these tools, please ensure you have opened this file with Adobe Reader DC, available for free at get.adobe.com/reader or by going to Help > Check for Updates within other versions of Reader. For more detailed instructions, please see us.sagepub.com/ReaderXProofs.

No.	Query
	Please confirm that all author information, including names, affiliations, sequence, and contact details, is correct.
	Please review the entire document for typographical errors, mathematical errors, and any other necessary corrections; check headings, tables, and figures.
	Please confirm that the Funding and Conflict of Interest statements are accurate.
	Please ensure that you have obtained and enclosed all necessary permissions for the reproduction of artistic works, (e.g. illustrations, photographs, charts, maps, other visual material, etc.) not owned by yourself. Please refer to your publishing agreement for further information.
	Please note that this proof represents your final opportunity to review your article prior to publication, so please do send all of your changes now.

Original Article

Institution of MECHANICAL ENGINEERS
Journal of MECHANICAL ENGINEERING SCIENCE

Proc IMechE Part C:
J Mechanical Engineering Science
0(0) 1–19

DOI: 10.1177/0954406217705906
journals.sagepub.com/home/pic
SAGE

Fault features analysis of a compound planetary gear set with damaged planet gears

Guoyan Li, Fangyi Li, Haohua Liu and Dehao Dong

Abstract

The fault properties of compound planetary gear set are much more complicated than the simple planetary gear set. A damaged planet will induce two periodic transient impulses in the raw signals and generates modulation sidebands around the mesh harmonics. This paper aims to investigate the fault properties of a compound planetary gear set in damaged planet conditions. A dynamic model is proposed to simulate the vibration signals. The time interval between the fault-induced close impulses in the time domain is used as a significant feature to locate the faulty planet. Considering the phase relations, the time-varying mesh stiffness is obtained. Then, the fault properties are demonstrated in the simulation, and the theoretical derivations are experimentally verified.

Keywords

Compound planetary gear set, nonlinear dynamic model, time-varying mesh stiffness, fault features, damaged planet

Date received: 14 September 2016; accepted: 27 March 2017

Introduction

Planetary gearboxes are widely used in large-scale and complex mechanical equipments, such as wind turbines, helicopters, and construction machineries. The fault forms of the gearboxes are diverse after a long-term service under tough operating conditions. Therefore, it is essential to assess the fault status of the gearboxes in order to provide useful information for the maintenance.

Local fault detection in gears based on the vibration analysis has been widely studied in many literature. Many important research topics have been proposed, including mathematical signal models,[1–5] model-based simulation,[6–18] advanced signal processing methods,[19,20] and fault features extraction.[21–25]

Most studies are focused on fault-induced impulses detection in the vibrations and modulation sidebands analysis in the spectra. The contacts of the damaged tooth area with the mating gears will cause impulses in the vibration. Such impulses appear periodically as the damaged gear rotates, and modulate the gear mesh vibrations at a repeating frequency, which is the fault characteristic frequency of the damaged gear.[2–4] The modulation generates sidebands around the mesh harmonics spacing at the fault characteristic frequency of the damaged gear in the spectrum.[2–4] All these can be used as significant fault characteristics to diagnose a faulty gear in a planetary gear set.

Assaad et al.[19] combined the time synchronous average (TSA) with the autoregressive model (AR) to assess the wear status of a planetary gear box. Barszcz et al.[20] used the spectral kurtosis to detect the weak impulses induced by a cracked ring gear. McFadden et al.[1] studied the modulation sidebands induced by the carrier rotation. Inalpolat and Kahraman[5] also proposed an analytical model to exhibit the sideband behaviors caused by the carrier rotation. Later, they[6] proposed a dynamic model to seek the fundamental understanding of the mechanisms of modulation sidebands induced by the gear manufacturing error of the planetary gear set. Cheng et al.[7,8] used the grey relational analysis (GRA) to estimate the crack levels and chip levers of the sun gear based on the dynamic simulation. Liang et al.[9] used model-based method to evaluate the effects of the crack propagation of the sun gear on the TVMS and investigated the fault characteristics of the cracked sun gear. Lei et al.[21] utilized the adaptive stochastic resonance (ASR) method to

Ministry of Education Key Laboratory of High-efficiency and Clean Mechanical Manufacture, School of Mechanical Engineering, Shandong University, Jinan, China

Corresponding author:
Fangyi Li, School of Mechanical Engineering, Shandong University, Jinan 250061, China.
Email: lifangyi@sdu.edu.cn

extract the fault characteristics of a planetary gear set when a chipped tooth or a missing tooth took place on the sun gear. Then, Lei et al.[22] proposed a multiclass relevance vector machine (mRVM) to distinguish the health conditions of the planetary gear set, and two features, the accumulative amplitudes of carrier order (AACO) and the energy ratio based on difference spectra (ERDS) proposed in Lei et al.,[23] were used as the inputs of the classifier. Further, Lei et al.[26] reviewed the studies of the fault diagnosis of planetary gear box in recent years. All these studies are helpful to understand the fault properties of planetary gearboxes.

Planet gears are the most abundant gear components in the planetary gearbox, which usually operate under tough environment and easily suffer from damages such as wear, pitting, chipping, cracking, and breakage.[2,21,22,26] Feng et al.[2] proposed the mathematical signal model to describe the modulation sidebands for a planetary gear set with damaged planet gear. In this study, they calculated the fault characteristic frequencies of the planet gear both in local and distributed damage cases, and analyzed the experimental signals collected from the gearbox with manual pitted planets. In another paper, Feng et al.[3] proposed joint amplitude and frequency demodulation method to illustrate the fault properties of faulty planet gear in the demodulated spectra. To eliminate the influence of transmission path, Feng et al.[4] illustrated the fault features of the planet gear in the demodulated spectra via torsional signals analysis. In this study, three local planet damage cases were considered: one tooth missing, a sun gear side crack, and a ring gear side crack. Chen and Shao[10] investigated the dynamic responses of a planetary gear set when a sun gear side crack took place on the planet gear, and the crack considered different crack sizes and inclination angles. Later, the effect of the tooth root crack and the tooth plastic inclination deformation on the dynamic responses of the planetary gear system are analyzed.[11] Further, they[12] took the ring gear flexibility and the tooth root crack into consideration and studied the dynamic features. Liang et al.[13] evaluated the effects of the crack on the TVMS when a sun gear side or a ring gear side crack took place on the planet gear. Then, they[14] studied the vibration properties of a planetary gear set with the sun gear side tooth crack on the planet gear. Furthermore, they[15] proposed a windowing and mapping strategy to detect the ring gear side tooth crack of the planet gear. Qu et al.[24] used the SVM-based feature selection method to assess the pitting degrees of the planet gear of a planetary gear set. Liu et al.[25] combined the kernel feature selection method with the kernel Fisher discriminant analysis (KFDA) to assess the pitting levels of the planet gear of a planetary gear set.

It is noticed that most studies were limited to the damage on one side of the planet tooth. However, the planet gear simultaneously meshes with the sun gear, ring gear, or other mating gears. Thus, the defects could practically take place on both sides of the planet tooth. The fault properties of the planet gear with defects on both tooth sides need further investigation. Tooth breakage is one common failure mode taking place on both sides of a gear tooth in a gear transmission. Therefore, we suppose one tooth missing takes place on the planet gear and investigate the fault properties of the damaged planet gear in this study.

It is also noticed that most studies are limited to the simple planetary gear set with fixed ring gear. However, compound planetary gear sets are more common in automatic transmissions, which can be used to implement complex transmissions. Kahraman,[27] Inalpolat and Kahraman,[28] Kiracofe and Parker,[29] and Guo and Parker[30–32] defined the compound planetary gear set as the gear set involving one or more of the following structures: meshed-planet, stepped-planet, and multistage planetary gear set. Kahraman[27] initially established a purely rotational model to investigate the modal properties of a meshed-planet gear set. Then, Inalpolat and Kahraman[28] developed a rotational model of general compound planetary gear set and demonstrated the dynamic behaviors of a three-stage planetary gear set. Kiracofe and Parker[29] developed the three-dimensional dynamic model of general compound planetary gear sets and investigated the modal properties of the gear system. Guo and Parker[30] developed a purely rotational model for general compound planetary gear sets to demonstrate the structured vibration properties, and then analyzed the relative mesh phase relations of the gear system.[32] In these studies, the gear mesh stiffness was considered as constant or square function. Moreover, these studies were mainly focused on the structural vibration properties of the healthy gear system, and no gear damages were considered in their models. Therefore, the fault properties of the compound planetary gear set should be further investigated.

In this research, we focus on a compound planetary gear set used in industrial gearboxes. As presented in Figure 1, the gear set consists of two gear stages and are connected via a common carrier c. The ring gears are made into one part denoted as r. The first gear stage is a simple planetary gear set with N planets $\dot{p}_i$ ($N = 3$). Each planet $\dot{p}_i$ is in mesh with the sun gear s_1 and the left part of the ring gear r. The second gear stage is a meshed-planet planetary gear set and has N planet–planet mesh pairs $\bar{p}_i - \hat{p}_i$ ($N = 3$). Each $\bar{p}_i - \hat{p}_i$ mesh pair is meshed both with the sun gear s_2 and the right part of the ring gear r. All the planets have the same design parameters. They are equally spaced on the carrier and supported through the planet shafts and needle roller bearings. In this transmission, the sun gear s_1 is locked, and the torque is transmitted from the input shaft to the sun gear s_2 via the spline, then from the sun gear to the planet carrier c.

Overall, there are three groups of planets in this gear set. For each group of planets, the damaged tooth will induce two close transient impulses at a

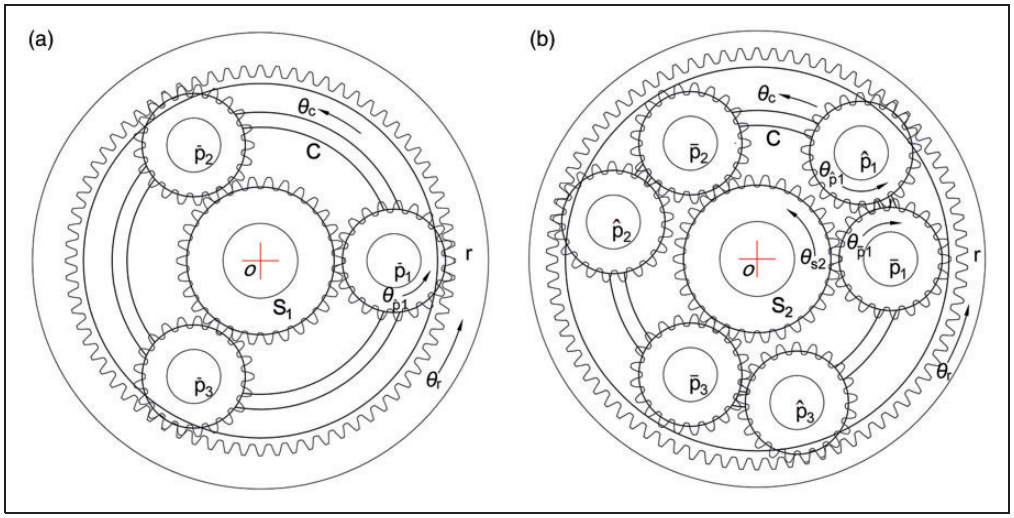

Figure 1. Compound planetary gear set: (a) the first gear stage, (b) the second gear stage.

special time interval in the raw signals. In addition, the spectral components could include close mesh harmonics with their surrounding sidebands for each gear stage. Moreover, the fault characteristic frequency of each group of planets would be quite close or identical. These all make the fault diagnosis of a compound planetary gear set in local planet damage cases more difficult than that of the simple planetary gear set.

Compared with experimental and industrial systems, dynamic simulation can separate the studied gears from others and eliminate the back noise, so the pattern of weak transient impulses can be identified accurately; we can also focus on the main factors that generate the modulation properties. Therefore, model-based dynamic analysis could be an important method to illustrate the theoretical fault features of a complex planetary gear set. However, published studies on model-based fault diagnosis of compound planetary gear set are limited.

As analyzed above, our main goal is to investigate the fault properties of the compound planetary gear set in damaged planet cases using model-based method. First, we propose a three-dimensional dynamic model for the gear set. Next, a mathematical method is used to calculate the time interval of damaged planet tooth in meshing. Incorporating such time intervals as well as the mesh phase relations, the total TVMS are evaluated. Further, the simulation signals are used to illustrate the fault features of planets. Finally, the experimental signals are analyzed to validate the theoretical analysis.

Dynamic model of the compound planetary gear set

Model overview

A lumped-parameter dynamic model is presented in Figure 2. Overall, there are 13 components in this gear set. We use j to represent the central components s_1, s_2, r, c and the planet gears p_i. We also use g to represent (1) the gear meshes between a central gear and a planet: $s_1 - \dot{p}_i$, $r - \dot{p}_i$, $s_2 - \bar{p}_i$, $r - \hat{p}_i$ and (2) the meshes between two planets $\bar{p}_i - \hat{p}_i$. Each component is allowed to translate in x and $y$directions and rotate around the axis based on a fixed absolute coordinate frame, denoted by x_j, y_j, and θ_j. All the components are assumed to be ideal rigid body with the mass m_j and the mass moment of inertia I_j. The gear meshes are modeled by spring-damping structures. The TVMS k_g and the viscous mesh damping coefficient c_g will be illustrated later. The spring-damping structures are also adopted to represent the supports, where k_{bj} and c_{bj} denote the radial stiffness and damping coefficient, respectively. k_{uj} and c_{uj} are the torsional support stiffness and damping coefficient, respectively. The influence of the tooth surface friction, tooth backlash, and tooth profile modifications on the dynamic responses are not covered in this paper. This will be our future work. When all these factors are taken into account, the nonlinear dynamic responses will be much more complicated. This may make it more difficult to extract the weak fault features.

Equations of motion

Before the derivation, $u_j = r_j\theta_j$ is defined as the rotational displacement in place of θ_j, where the r_j ($j = s_1$, s_2, r, p) are the base radii of gears, and r_c is the distance passing the planet center.

The gear mesh force for each mesh pair g is defined as

$$F_g = c_g\dot{\delta}_g + k_g\delta_g \tag{1}$$

where δ_g is the relative gear mesh displacement along the line of action.

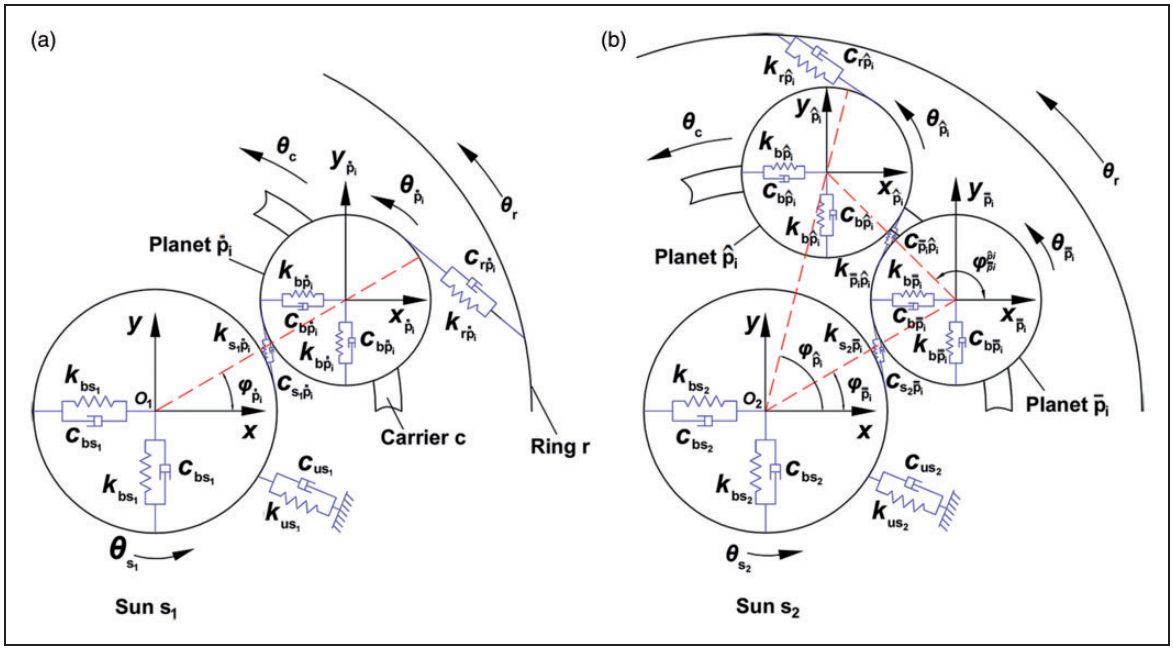

Figure 2. Dynamic model of the compound planetary gear set: (a) the first gear stage, (b) the second gear stage.

F_{bjx}, F_{bjy}, and F_{uj} represent the bearing forces in x, y, and u directions, respectively, which can be expressed as

$$\begin{cases} F_{bjx} = c_{bj}\dot{x}_j + k_{bj}x_j \\ F_{bjy} = c_{bj}\dot{y}_j + k_{bj}y_j \\ F_{uj} = c_{uj}\dot{u}_j + k_{uj}u_j \end{cases} \tag{2}$$

The equations of motion for the gear pair subsystem are derived as[17]

$$\begin{cases} m_{s_1}\ddot{x}_{s_1} - \sum_{i=1}^{N} \sin\varphi_{s_1\dot{p}_i} F_{s_1\dot{p}_i} + F_{bs_1x} = 0 \\ m_{s_1}\ddot{y}_{s_1} + \sum_{i=1}^{N} \cos\varphi_{s_1\dot{p}_i} F_{s_1\dot{p}_i} + F_{bs_1y} = 0 \\ \frac{I_{s_1}}{r_{s_1}^2}\ddot{u}_{s_1} + \sum_{i=1}^{N} F_{s_1\dot{p}_i} + F_{us_1} = 0 \end{cases} \tag{3}$$

$$\begin{cases} m_{s_2}\ddot{x}_{s_2} - \sum_{i=1}^{N} \sin\varphi_{s_2\bar{p}_i} F_{s_2\bar{p}_i} + F_{bs_2x} = 0 \\ m_{s_2}\ddot{y}_{s_2} + \sum_{i=1}^{N} \cos\varphi_{s_2\bar{p}_i} F_{s_2\bar{p}_i} + F_{bs_2y} = 0 \\ \frac{I_{s_2}}{r_{s_2}^2}\ddot{u}_{s_2} + \sum_{i=1}^{N} F_{s_2\bar{p}_i} + F_{us_2} = \frac{T_{\text{in}}}{r_{s_2}} \end{cases} \tag{4}$$

$$\begin{cases} m_r\ddot{x}_r + \sum_{i=1}^{N} \sin\varphi_{r\hat{p}_i} F_{r\hat{p}_i} - \sum_{i=1}^{N} \sin\varphi_{r\dot{p}_i} F_{r\dot{p}_i} + F_{brx} = 0 \\ m_r\ddot{y}_r - \sum_{i=1}^{N} \cos\varphi_{r\hat{p}_i} F_{r\hat{p}_i} + \sum_{i=1}^{N} \cos\varphi_{r\dot{p}_i} F_{r\dot{p}_i} + F_{bry} = 0 \\ \frac{I_r}{r_r^2}\ddot{u}_r - \sum_{i=1}^{N} F_{r\hat{p}_i} + \sum_{i=1}^{N} F_{r\dot{p}_i} + F_{ur} = 0 \end{cases} \tag{5}$$

$$\begin{cases} m_{\dot{p}_i}\ddot{x}_{\dot{p}_i} + \sin\varphi_{s_1\dot{p}_i} F_{s_1\dot{p}_i} + \sin\varphi_{r\dot{p}_i} F_{r\dot{p}_i} = 0 \\ m_{\dot{p}_i}\ddot{y}_{\dot{p}_i} - \cos\varphi_{s_1\dot{p}_i} F_{s_1\dot{p}_i} - \cos\varphi_{r\dot{p}_i} F_{r\dot{p}_i} = 0 \\ \frac{I_{\dot{p}_i}}{r_{\dot{p}_i}^2}\ddot{u}_{\dot{p}_i} + F_{s_1\dot{p}_i} - F_{r\dot{p}_i} = 0 \end{cases} \tag{6}$$

$$\begin{cases} m_{\bar{p}_i}\ddot{x}_{\bar{p}_i} + \sin\varphi_{\bar{p}_i\hat{p}_i} F_{\bar{p}_i\hat{p}_i} + \sin\varphi_{s_2\bar{p}_i} F_{s_2\bar{p}_i} = 0 \\ m_{\bar{p}_i}\ddot{y}_{\bar{p}_i} - \cos\varphi_{\bar{p}_i\hat{p}_i} F_{\bar{p}_i\hat{p}_i} - \cos\varphi_{s_2\bar{p}_i} F_{s_2\bar{p}_i} = 0 \\ \frac{I_{\bar{p}_i}}{r_{\bar{p}_i}^2}\ddot{u}_{\bar{p}_i} + F_{s_2\bar{p}_i} - F_{\bar{p}_i\hat{p}_i} = 0 \end{cases} \tag{7}$$

$$\begin{cases} m_{\hat{p}_i}\ddot{x}_{\hat{p}_i} - \sin\varphi_{\bar{p}_i\hat{p}_i} F_{\bar{p}_i\hat{p}_i} - \sin\varphi_{r\hat{p}_i} F_{r\hat{p}_i} = 0 \\ m_{\hat{p}_i}\ddot{y}_{\hat{p}_i} + \cos\varphi_{\bar{p}_i\hat{p}_i} F_{\bar{p}_i\hat{p}_i} + \cos\varphi_{r\hat{p}_i} F_{r\hat{p}_i} = 0 \\ \frac{I_{\hat{p}_i}}{r_{\hat{p}_i}^2}\ddot{u}_{\hat{p}_i} - F_{\bar{p}_i\hat{p}_i} + F_{r\hat{p}_i} = 0 \end{cases} \tag{8}$$

For the gear meshes between a central gear and a planet, we can get $\varphi_g = \varphi_{p_i} - \lambda\alpha$, where φ_{p_i} ($p_i = \dot{p}_i, \bar{p}_i, \hat{p}_i$) is the spacing angle of planet with respect to the carrier center, which can be expressed as: $\varphi_{\dot{p}_i} = \frac{2\pi(i-1)}{N}$ (for the planets in the first gear stage), $\varphi_{\bar{p}_i} = \frac{2\pi(i-1)}{N}$ (for the planets meshed with sun gear in the second gear stage), and $\varphi_{\hat{p}_i} = \frac{2\pi(i-1)}{N} + 45^\circ$ (for the planets meshed with ring gear in the second gear stage); $\lambda = -1$ for the $r - \dot{p}_i$ mesh pair and $\lambda = 1$ for the $r - \hat{p}_i$, $s_1 - \dot{p}_i$, and $s_2 - \bar{p}_i$ mesh pairs; α is the pressure angle. For the gear meshes between two planets, we can obtain $\varphi_g = \varphi_{\bar{p}_i}^{\hat{p}_i} - \lambda\alpha$, where $\varphi_{\bar{p}_i}^{\hat{p}_i}$ is the spacing angle of planet $\hat{p}_i$ with respect to the planet $\bar{p}_i$ and expressed as: $\varphi_{\bar{p}_1}^{\hat{p}_1} = \frac{2\pi(i-1)}{N} + 105^\circ$, and $\lambda = -1$ for the $\bar{p}_i - \hat{p}_i$ mesh pair.

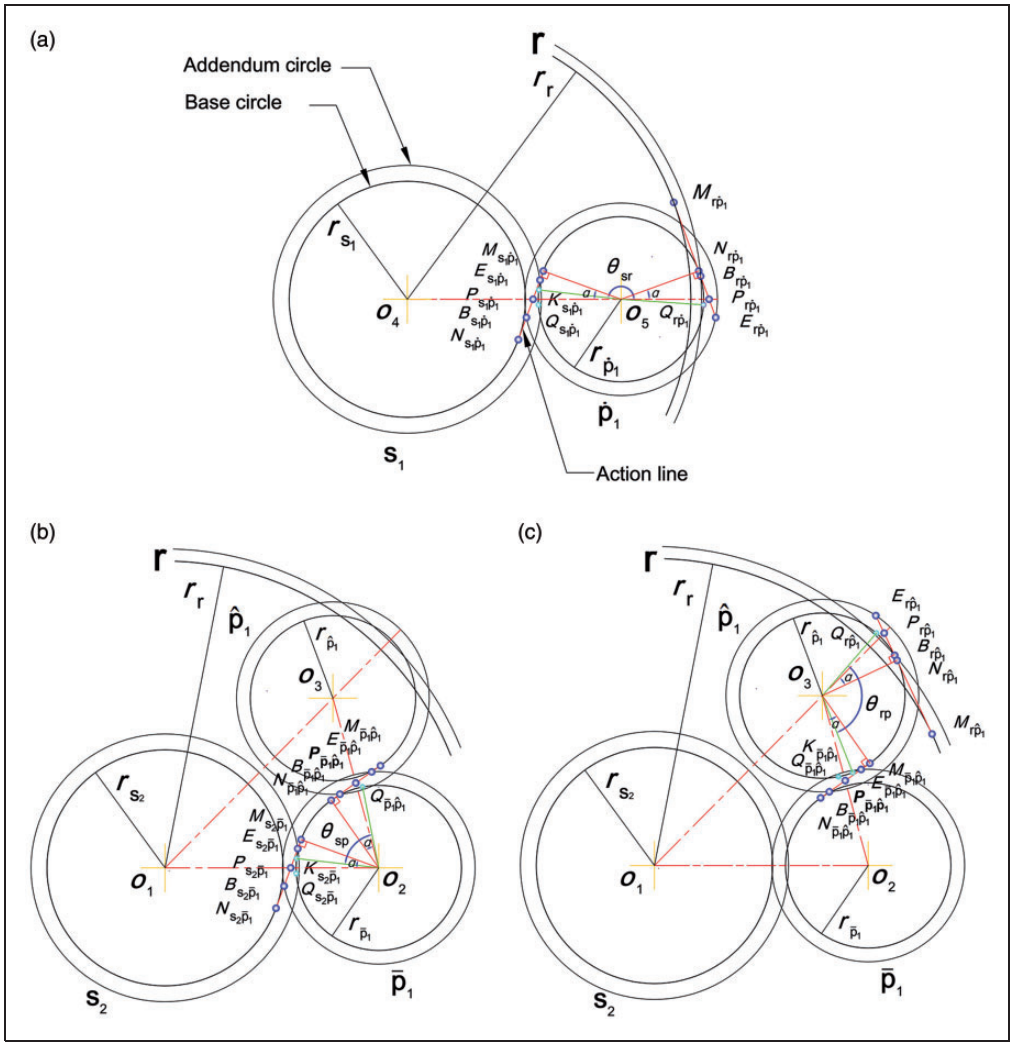

Figure 3. Mesh sketch of the compound planetary gear set: (a) the first case, (b) the second case, (c) the third case.

The equations of motion for carrier-planet subsystem are expressed as[17]

$$\begin{cases} m_c\ddot{x}_c+\sum_{i=1}^{N}\left(c_{bp_i}\dot{\delta}_{cp_ix}+k_{bp_i}\delta_{cp_ix}\right)+\left(c_{bc}\dot{x}_c+k_{bc}x_c\right)=0 \\ m_c\ddot{y}_c+\sum_{i=1}^{N}\left(c_{bp_i}\dot{\delta}_{cp_iy}+k_{bp_i}\delta_{cp_iy}\right)+\left(c_{bc}\dot{x}_c+k_{bc}x_c\right)=0 \\ \frac{I_c}{r_c^2}-\sum_{i=1}^{N}\left(c_{bp_i}\dot{\delta}_{cp_ix}+k_{bp_i}\delta_{cp_ix}\right)\sin\varphi_{p_i} \\ +\sum_{i=1}^{N}\left(c_{bp_i}\dot{\delta}_{cp_iy}+k_{bp_i}\delta_{cp_iy}\right)\cos\varphi_{p_i} \\ +\left(c_{uc}\dot{u}_c+k_{uc}u_c\right)=-\frac{T_{\text{out}}}{r_c} \end{cases} \tag{9}$$

$$\begin{cases} m_{p_i}\ddot{x}_{p_i}-\left(c_{bp_i}\dot{\delta}_{cp_ix}+k_{bp_i}\delta_{cp_ix}\right)=0 \\ m_{p_i}\ddot{y}_{p_i}-\left(c_{bp_i}\dot{\delta}_{cp_iy}+k_{bp_i}\delta_{bp_iy}\right)=0 \end{cases} \tag{10}$$

in these equations, δ_{cp_ix} and δ_{cp_iy} are the relative displacements between carrier and planets in x_c and y_c directions. T_{out} is the output load torque.

Overall, the system matrix can be assembled as

$$\mathbf{M}\ddot{\mathbf{Q}}(t)+(\mathbf{C_m}+\mathbf{C_b})\dot{\mathbf{Q}}(t)+(\mathbf{K_m}+\mathbf{K_b})\mathbf{Q}(t)=\mathbf{T} \tag{11}$$

where $\mathbf{M}$ is the inertia matrix, $\mathbf{Q}$ is the displacement matrix, $\mathbf{C_m}$ is the mesh damping matrix, $\mathbf{C_b}$ is the bearing damping matrix, $\mathbf{K_m}$ is the gear mesh stiffness matrix, $\mathbf{K_b}$ is the bearing stiffness matrix, is the external torque matrix. The detailed submatrices are provided in the appendix of Li et al.[17]

Time interval of the damaged planet tooth in meshing per revolution

The planet gear simultaneously meshes with the sun gear, ring gear, or other planet gear. Suppose that the damage exists on both sides of the planet tooth. The damaged area will contact with two mating gears sequentially per revolution, so two sudden changes will be caused at a special time interval in the vibration. It is essential to evaluate such time interval between fault-induced impulses since it could be an important signature to locate the faulty planet.

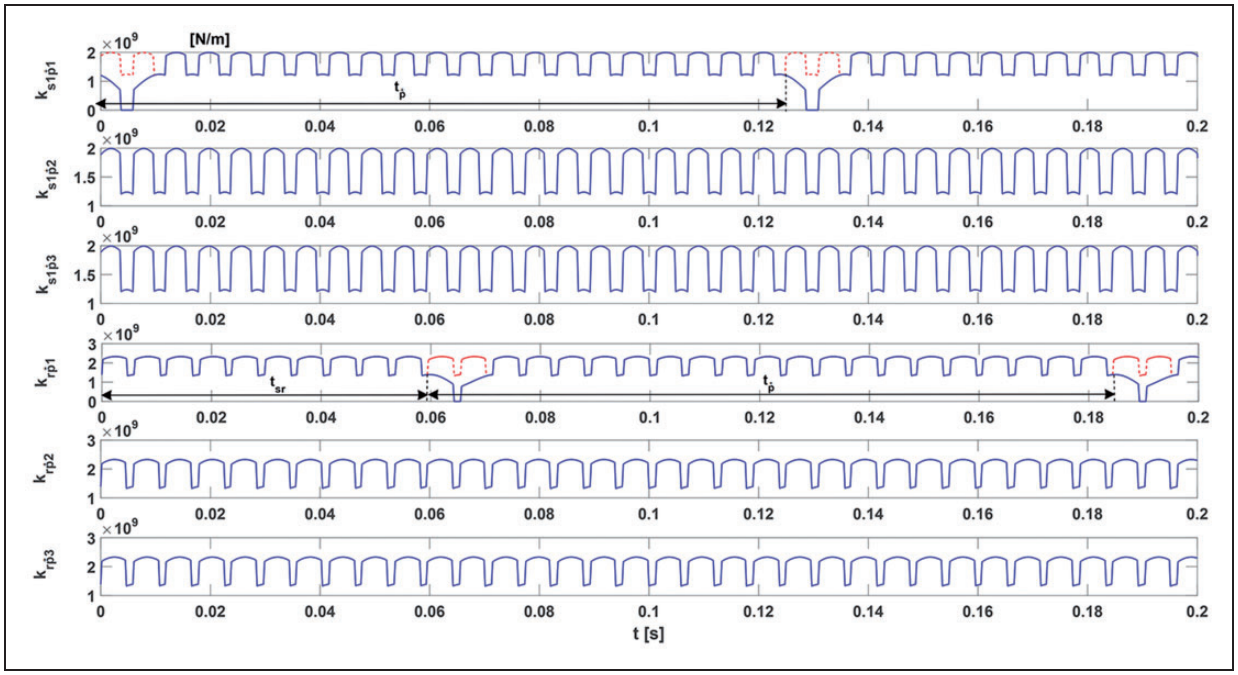

Figure 4. Mesh stiffness curves for the mesh pairs in the first gear stage in the case that one tooth missing occurs on $\dot{p}_1$.

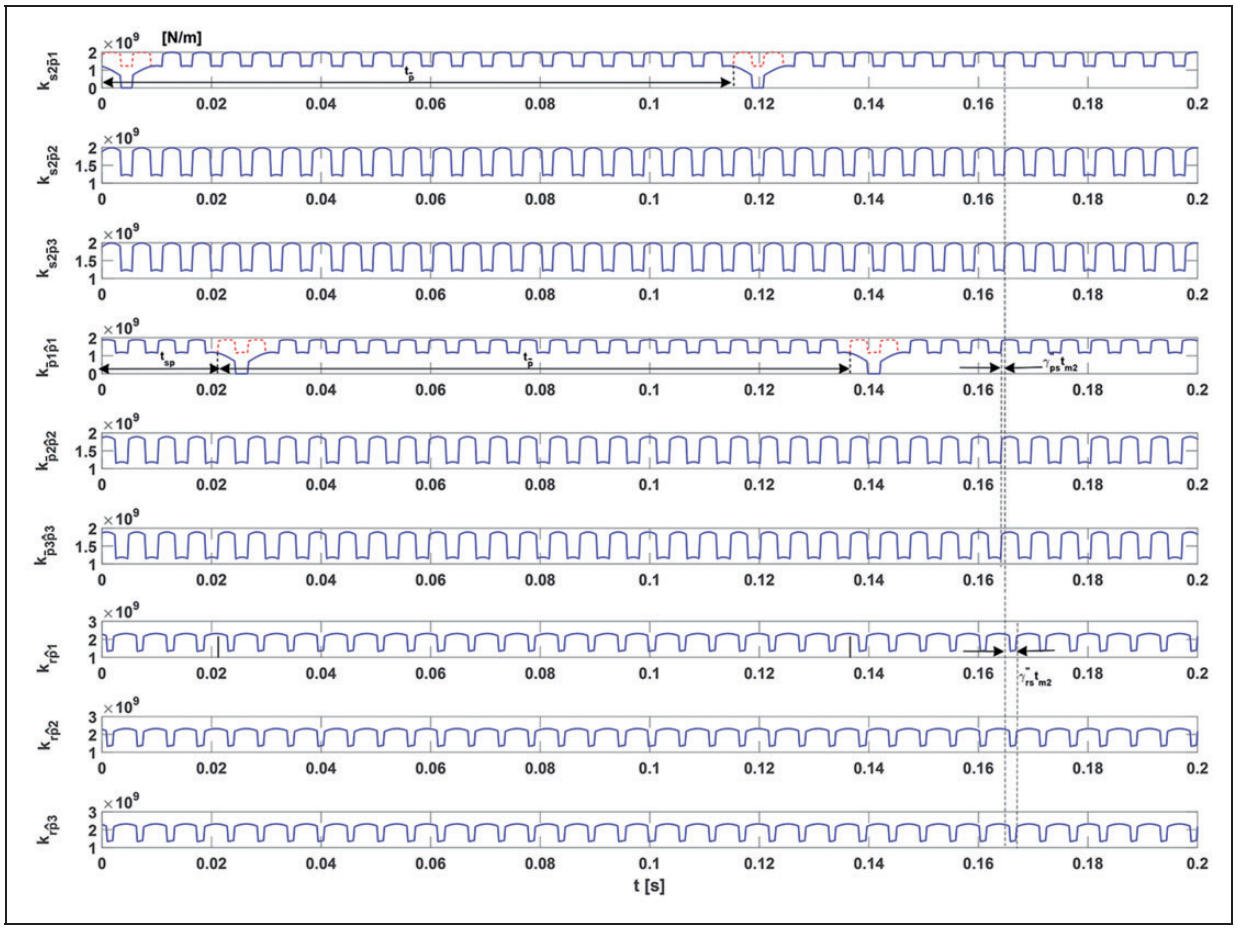

Figure 5. Mesh stiffness curves for the mesh pairs in the second gear stage in the case that one tooth missing occurs on $\bar{p}_1$.

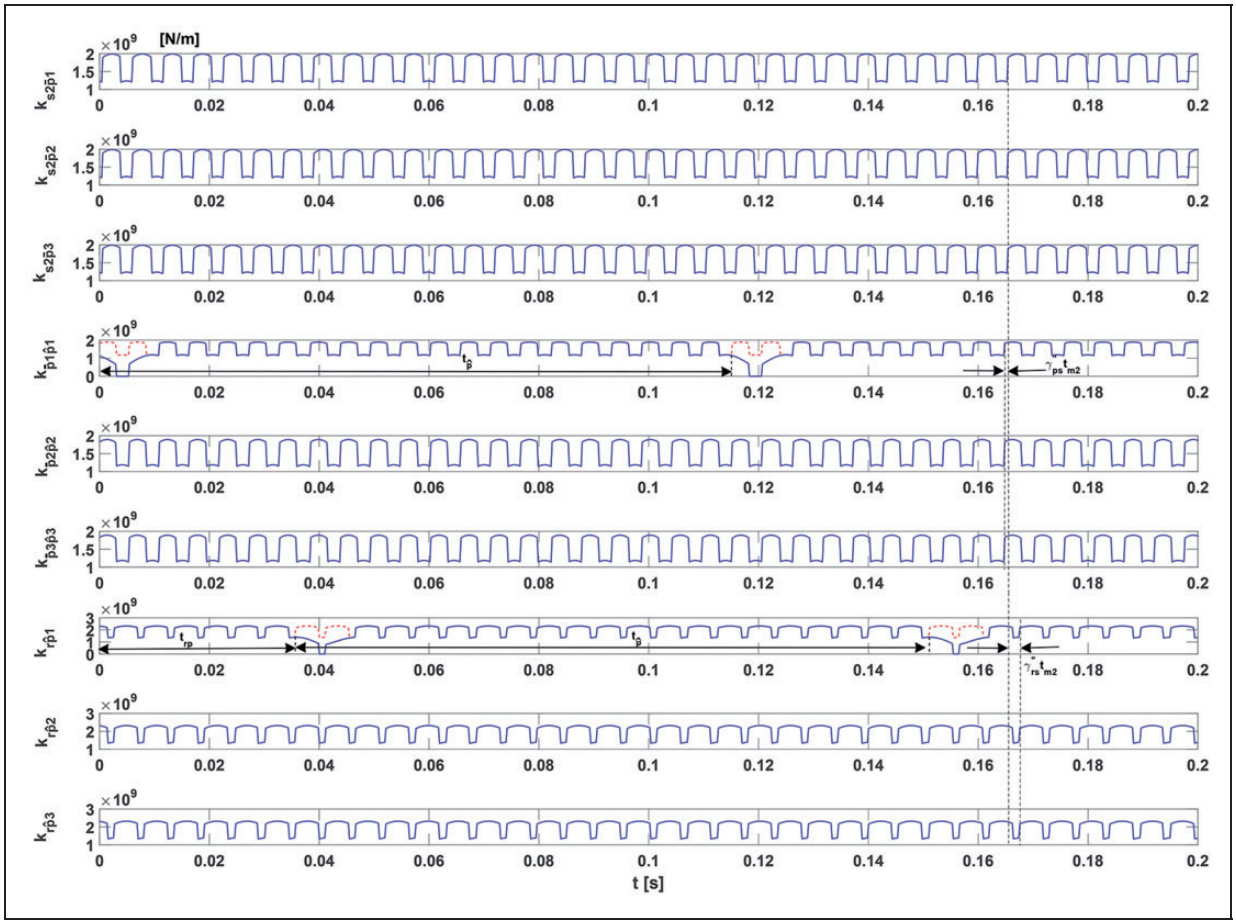

Figure 6. Mesh stiffness curves for the mesh pairs in the second gear stage in the case that one tooth missing occurs on $\hat{p}_1$.

Table 1. Time values provided in three broken planet cases.

	Stage 1	Stage 2	
	$\dot{p}_i$	$\bar{p}_i$	$\hat{p}_i$
Mesh period (s)	$t_{m1} = 0.0060$	$t_{m2} = 0.0055$	
Time interval of the damaged planet tooth in meshing (s)	$t_{sr} = 0.0595$	$t_{sp} = 0.0213$	$t_{rp} = 0.0358$
Period of the damaged planet tooth in meshing (s)	$t_{\dot{p}} = 0.1250$	$t_{\bar{p}} = 0.1149$	$t_{\hat{p}} = 0.1149$

The gear meshes can be classified as meshes between a central gear and a planet ($s_1 - \dot{p}_i$, $r - \dot{p}_i$, $s_2 - \bar{p}_i$, $r - \hat{p}_i$) and meshes between two planets ($\bar{p}_i - \hat{p}_i$). So, there are three groups of planets in this gear set: $\dot{p}_i$ that influences $s_1 - \dot{p}_i$ and $r - \dot{p}_i$ mesh pairs in the first gear stage, $\bar{p}_i$ that influences $s_2 - \bar{p}_i$ and $\bar{p}_i - \hat{p}_i$ mesh pairs in the second stage, and $\hat{p}_i$ that influences $\bar{p}_i - \hat{p}_i$ and $r - \hat{p}_i$ mesh pairs in the second gear stage. Overall, three local planet damage cases are considered here. Case (i): one tooth missing on $\dot{p}_1$; case (ii): one tooth missing on $\bar{p}_1$; and case (iii): one tooth missing on $\hat{p}_1$. The time intervals of the damaged tooth in meshing per revolution are denoted by t_{sr} for case (i), t_{sp} for case (ii), and t_{rp} for case (iii), respectively.

Case (i): One tooth missing on $\dot{p}_1$. As denoted in Figure 3(a), $\overline{N_{s_1\dot{p}_1}M_{s_1\dot{p}_1}}$ and $\overline{N_{r\dot{p}_1}M_{r\dot{p}_1}}$ represent the theoretical action lines, whereas $\overline{B_{s_1\dot{p}_1}E_{s_1\dot{p}_1}}$ and $\overline{B_{r\dot{p}_1}E_{r\dot{p}_1}}$ represent the practical action lines for the mesh pairs $s_1 - \dot{p}_1$ and $r - \dot{p}_1$, respectively. To calculate t_{sr}, we set the mesh pair $s_1 - \dot{p}_1$ as the reference mesh for the mesh pair $r - \dot{p}_1$ and suppose that the damaged tooth on the planet $\dot{p}_1$ is in mesh with the sun gear s_1 at the pitch point $P_{s_1\dot{p}_1}$. For convenience, this point is chosen as the reference point to begin the

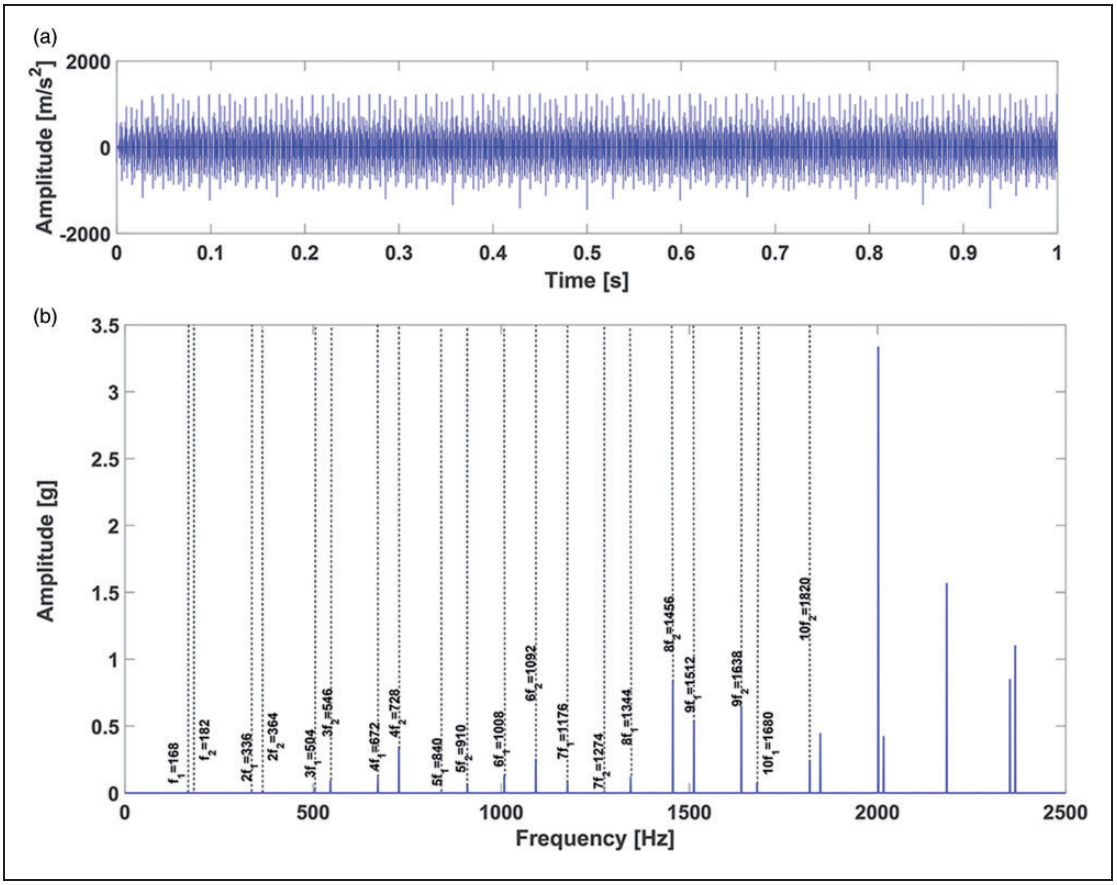

Figure 7. (a) Simulated signal and (b) Fourier spectrum for the healthy gear set.

calculation. It is noted that the choice of the reference point is arbitrary in the mesh duration of the damaged tooth and will not affect the results that follow. After t_{sr}, the damaged tooth on the planet $\dot{p}_1$ will rotate to mesh with the ring gear at the pitch point $P_{r\dot{p}_1}$, which is called the associated mesh point.

According to the assumption above, there are two important factors determining t_{sr}: (1) the rotation speed of the damaged planet relative to the carrier denoted as $n_{\dot{p}_1 c}$ in rpm and (2) the rotation angle θ_{sr} in rad, at which the damaged tooth rotates from contact region of reference mesh pair to the contact region of referring mesh pair.

In order to calculate the rotation angle θ_{sr}, we need to calculate the corresponding arc length. First, it is necessary to wrap the action lines $\overline{N_{s_1\dot{p}_1}M_{s_1\dot{p}_1}}$ and $\overline{N_{r\dot{p}_1}M_{r\dot{p}_1}}$ on the base circle of $\dot{p}_1$, and then define the corresponding point of $P_{s_1\dot{p}_1}$ as point $Q_{s_1\dot{p}_1}$ and the corresponding point of $P_{r\dot{p}_1}$ as point $Q_{r\dot{p}_1}$. It is noted that the mesh pair $r-\dot{p}_1$ meshes on the opposite tooth surface of the planet with respect to the $s_1-\dot{p}_1$ mesh pair, so we need to define another point $K_{s_1\dot{p}_1}$ as the beginning point of this arc length rather than the point $Q_{s_1\dot{p}_1}$, from which the arc length to point $Q_{s_1\dot{p}_1}$ is $s_{b\dot{p}_1}$, where $s_{b\dot{p}_1}$ is the tooth thickness of the planet $\dot{p}_1$ on the base circle. Thus, the time interval t_{sr} is calculated as

$$t_{sr}=\frac{\theta_{sr}}{\frac{n_{\dot{p}_1 c}}{60}\times 360}=\frac{\frac{\widehat{K_{s_1\dot{p}_1}Q_{r\dot{p}_1}}}{r_{\dot{p}_1}}\times\frac{180}{\pi}}{\frac{n_{\dot{p}_1 c}}{60}\times 360}=\frac{30\widehat{K_{s_1\dot{p}_1}Q_{r\dot{p}_1}}}{r_{\dot{p}_1}\pi n_{\dot{p}_1 c}} \tag{12}$$

Based on the mesh sketch illustrated in Figure 3(a)

$$\begin{aligned}&\widehat{K_{s_1\dot{p}_1}Q_{r\dot{p}_1}}\\&=\widehat{Q_{s_1\dot{p}_1}M_{s_1\dot{p}_1}}-\widehat{s_{b\dot{p}_1}}+\widehat{M_{s_1\dot{p}_1}N_{r\dot{p}_1}}+\widehat{N_{r\dot{p}_1}Q_{r\dot{p}_1}}\\&=\overline{P_{s_1\dot{p}_1}M_{s_1\dot{p}_1}}-\widehat{s_{b\dot{p}_1}}+\widehat{M_{s_1\dot{p}_1}N_{r\dot{p}_1}}+\overline{N_{r\dot{p}_1}P_{r\dot{p}_1}}\\&=2r_{\dot{p}_1}\tan\alpha-\widehat{s_{b\dot{p}_1}}+r_{\dot{p}_1}(\pi-2\alpha)\end{aligned} \tag{13}$$

Case (ii): One tooth missing on $\bar{p}_1$. Similarly, as denoted in Figure 3(b), point $P_{s_2\bar{p}_1}$ represents the reference point in the $s_2-\bar{p}_1$ mesh region ($\overline{B_{s_2\bar{p}_1}E_{s_2\bar{p}_1}}$), and point $P_{\bar{p}_1\hat{p}_1}$ represents the associated mesh point in the $\bar{p}_1-\hat{p}_1$contact region ($\overline{B_{\bar{p}_1\hat{p}_1}E_{\bar{p}_1\hat{p}_1}}$). Then, we wrap $\overline{B_{s_2\bar{p}_1}E_{s_2\bar{p}_1}}$ and $\overline{B_{\bar{p}_1\hat{p}_1}E_{\bar{p}_1\hat{p}_1}}$ on the base circle of $\bar{p}_1$ and define the corresponding points $Q_{s_2\bar{p}_1}$, $Q_{\bar{p}_1\hat{p}_1}$, and $K_{s_2\bar{p}_1}$. Thus, the time interval t_{sp} is expressed as

$$t_{sp}=\frac{\theta_{sp}}{\frac{n_{\bar{p}_1 c}}{60}\times 360}=\frac{\frac{\widehat{K_{s_2\bar{p}_1}Q_{\bar{p}_1\hat{p}_1}}}{r_{\bar{p}_1}}\times\frac{180}{\pi}}{\frac{n_{\bar{p}_1 c}}{60}\times 360}=\frac{30\widehat{K_{s_2\bar{p}_1}Q_{\bar{p}_1\hat{p}_1}}}{r_{\bar{p}_1}\pi n_{\bar{p}_1 c}} \tag{14}$$

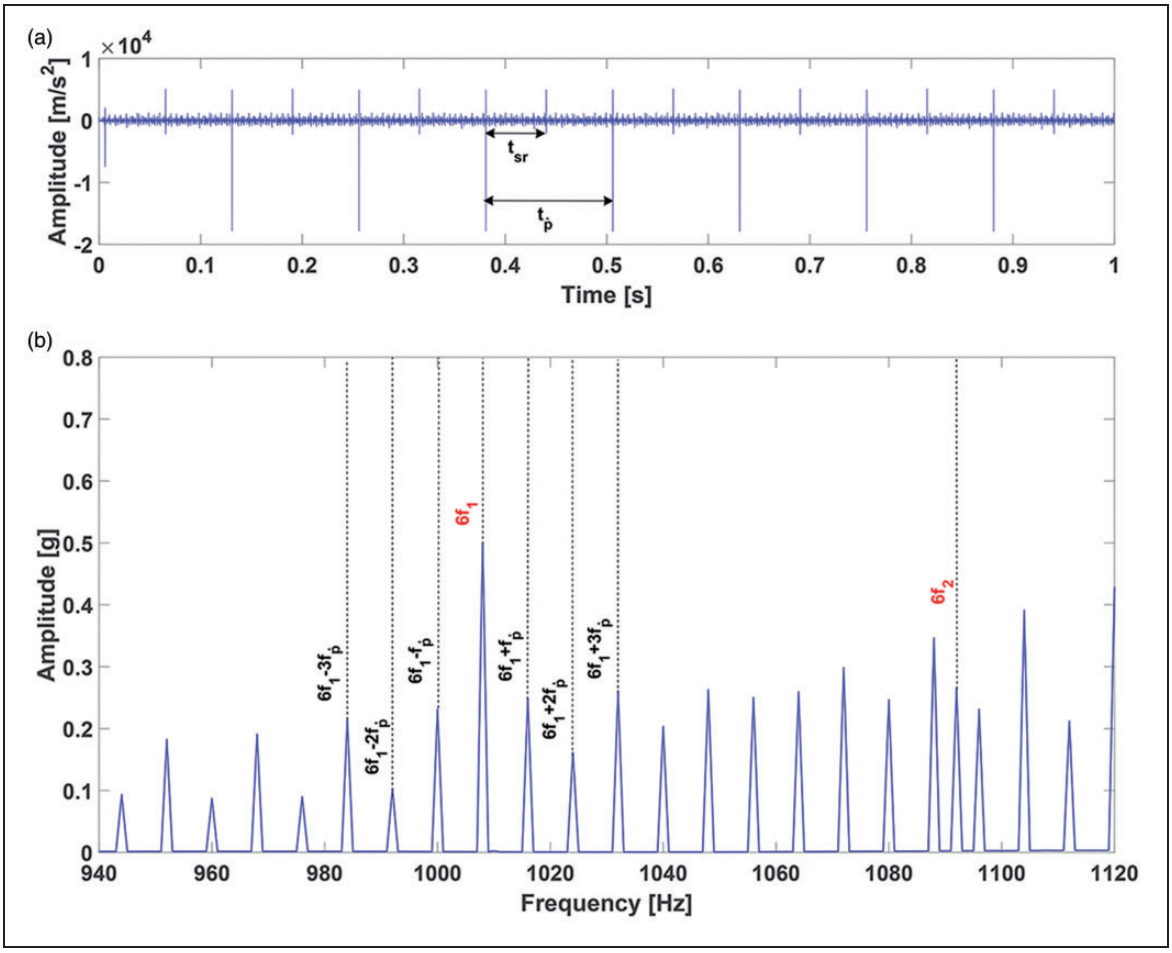

Figure 8. (a) Simulation signal and (b) zoomed-in Fourier spectrum for the gear set in the local broken planet $\dot{p}_1$ case.

where $\widehat{K_{s_2\bar{p}_1}Q_{\bar{p}_1\hat{p}_1}}$ is calculated as

$$\begin{aligned}&\widehat{K_{s_2\bar{p}_1}Q_{\bar{p}_1\hat{p}_1}}\\&=\widehat{Q_{s_2\bar{p}_1}M_{s_2\bar{p}_1}}-\widehat{s_{b\bar{p}_1}}+\widehat{M_{s_2\bar{p}_1}N_{s_2\bar{p}_1}}+\widehat{N_{s_2\bar{p}_1}Q_{\bar{p}_1\hat{p}_1}}\\&=\overline{P_{s_2\bar{p}_1}M_{s_2\bar{p}_1}}-\widehat{s_{b\bar{p}_1}}+\widehat{M_{s_2\bar{p}_1}N_{s_2\bar{p}_1}}+\overline{N_{s_2\bar{p}_1}P_{\bar{p}_1\hat{p}_1}}\\&=2r_{\bar{p}_1}\tan\alpha-\widehat{s_{b\bar{p}_1}}+r_{\bar{p}_1}(\angle O_1O_2O_3-2\alpha)\end{aligned}\quad(15)$$

Case (iii): One tooth missing on $\hat{p}_1$. As denoted in Figure 3(c), point $P_{\bar{p}_1\hat{p}_1}$ represents the reference mesh point in the $\bar{p}_1-\hat{p}_1$ mesh region ($\overline{B_{\bar{p}_1\hat{p}_1}E_{\bar{p}_1\hat{p}_1}}$), and point $P_{r\hat{p}_1}$ represents the associated mesh point in the $r-\hat{p}_1$ contact region ($\overline{B_{r\hat{p}_1}E_{r\hat{p}_1}}$). Likewise, we wrap $\overline{B_{\bar{p}_1\hat{p}_1}E_{\bar{p}_1\hat{p}_1}}$ and $\overline{B_{r\hat{p}_1}E_{r\hat{p}_1}}$ on the base circle of $\hat{p}_1$ and then define points $Q_{\bar{p}_1\hat{p}_1}$, $Q_{r\hat{p}_1}$, and $K_{\bar{p}_1\hat{p}_1}$. The equation to calculate t_{rp} is expressed as

$$t_{rp}=\frac{\theta_{rp}}{\frac{n_{\hat{p}_1c}}{60}\times 360}=\frac{\frac{\widehat{K_{\bar{p}_1\hat{p}_1}Q_{r\hat{p}_1}}}{r_{\hat{p}_1}}\times\frac{180}{\pi}}{\frac{n_{\hat{p}_1c}}{60}\times 360}=\frac{30\widehat{K_{\bar{p}_1\hat{p}_1}Q_{r\hat{p}_1}}}{r_{\hat{p}_1}\pi n_{\hat{p}_1c}}\quad(16)$$

where $\widehat{K_{\bar{p}_1\hat{p}_1}Q_{r\hat{p}_1}}$ is calculated as

$$\begin{aligned}\widehat{K_{\bar{p}_1\hat{p}_1}Q_{r\hat{p}_1}}&=\widehat{Q_{\bar{p}_1\hat{p}_1}M_{\bar{p}_1\hat{p}_1}}-\widehat{s_{b\hat{p}_1}}+\widehat{M_{\bar{p}_1\hat{p}_1}N_{r\hat{p}_1}}+\widehat{N_{r\hat{p}_1}Q_{r\hat{p}_1}}\\&=\overline{P_{\bar{p}_1\hat{p}_1}M_{\bar{p}_1\hat{p}_1}}-\widehat{s_{b\hat{p}_1}}+\widehat{M_{\bar{p}_1\hat{p}_1}N_{r\hat{p}_1}}+\overline{N_{r\hat{p}_1}P_{r\hat{p}_1}}\\&=2r_{\hat{p}_1}\tan\alpha-\widehat{s_{b\hat{p}_1}}+r_{\hat{p}_1}(\pi-\angle O_1O_3O_2-2\alpha)\end{aligned}\quad(17)$$

Evaluation of TVMS

The derivations of TVMS and the mesh phases are provided in our earlier work[17] and briefly summarized in Appendix 1.

Case (i): One tooth missing occurs on $\dot{p}_1$. Figure 4 presents the TVMS curves for $s_1-\dot{p}_i$ and $r-\dot{p}_i$ mesh pairs, respectively. Based on the mesh phase relations provided in Table 3 of Appendix 1, all the mesh pairs are in-phase with each other. It shows that the mesh period for the first gear stage, denoted as t_{m1}, is 0.0060 s. For the healthy mesh pair, the double-tooth mesh duration and single-tooth mesh duration occur in turn per mesh period. The proportion of each duration in one mesh period depends on the contact ratio of the corresponding mesh pair. This leads to normal and periodic mesh vibrations.

Assuming that the damaged tooth on $\dot{p}_1$ goes into mesh with the sun gear at $t=0$, the damaged tooth

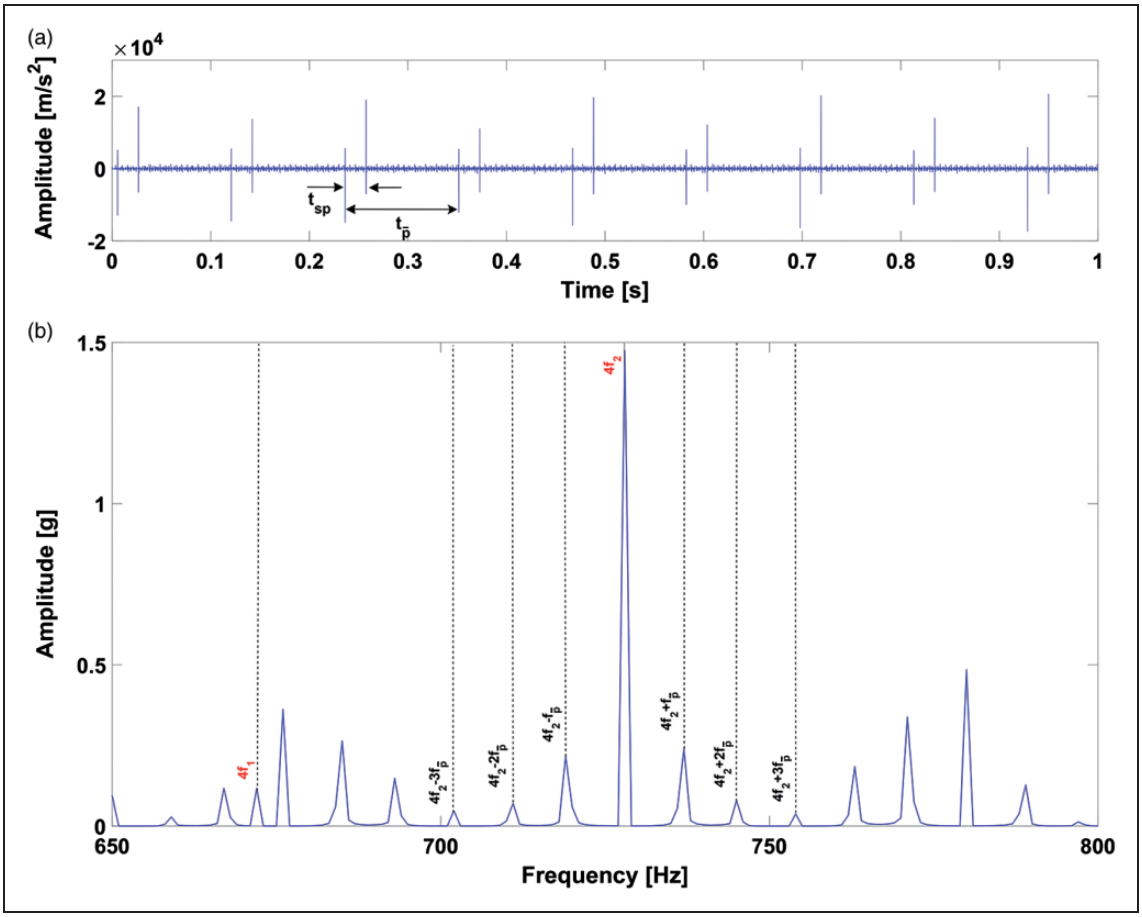

Figure 9. (a) Simulation signal and (b) zoomed-in Fourier spectrum for the gear set in the local broken planet $\bar{p}_1$ case.

loses contact in the double-tooth mesh duration, and there is even no mesh in the single-tooth mesh duration. Therefore, the TVMS of $s_1 - \dot{p}_1$ mesh pair decrease over the total mesh duration of this damaged tooth (1.61 mesh period), while other mesh pairs are not affected. Then, the damaged tooth meshes with the ring gear after $t_{sr} = 0.0595$s, so the TVMS of $r - \dot{p}_1$ mesh pair reduces obviously over 1.78 mesh period, while other mesh pairs are not affected. After one revolution, the damaged tooth meshes with the sun gear and the ring gear in turn again, so the reduction of the TVMS will occur in a repetition of 0.1250 s, denoted as $t_{\dot{p}}$, which only depends on the rotation speed of the damaged planet relative to the carrier.

Case (ii): One tooth missing occurs on $\bar{p}_1$. Figure 5 shows the TVMS curves for the $s_2 - \bar{p}_i$, $\bar{p}_i - \hat{p}_i$, and $r - \hat{p}_i$ mesh pairs in the second gear stage, respectively. It shows that the mesh period for this gear stage, denoted as t_{m2}, is 0.0055 s. The phases of $\bar{p}_i - \hat{p}_i$ mesh pairs lead to the $s_2 - \bar{p}_i$ mesh pairs, and the time difference is $\gamma''_{ps} t_{m2}$. The phases of $r - \hat{p}_i$ mesh pairs lag to the $s_2 - \bar{p}_i$ mesh pairs, and the time difference is $\gamma''_{rs} t_{m2}$. There are no phase differences between the ith $s_2 - \bar{p}_i$, $\bar{p}_i - \hat{p}_i$, or $r - \hat{p}_i$ mesh pairs. The broken planet tooth will mesh with the sun gear s_2 and $\hat{p}_1$ in turn per revolution, and the time interval t_{sp} is equal to 0.0213 s. Over the total mesh duration of the damaged tooth, the TVMS of $s_2 - \bar{p}_1$ and $\bar{p}_1 - \hat{p}_1$ mesh pairs reduce obviously, while others are not affected. The total mesh duration of the damaged tooth is 1.61 mesh period for $s_2 - \bar{p}_1$ mesh pair and 1.57 mesh period for $\bar{p}_1 - \hat{p}_1$ mesh pair. After one revolution, the damaged tooth will contact with the sun gear and planet in turn again, so the reduction of the TVMS occurs in a repetition of $t_{\bar{p}}$, which is 0.1149 s.

Case (iii): One tooth missing occurs on $\hat{p}_1$. The mesh phase relations in this case are the same as in case (ii). Likewise, the TVMS of $\bar{p}_1 - \hat{p}_1$ and $r - \hat{p}_1$ mesh pairs decrease obviously over the total mesh duration of the damaged tooth, which is 1.57 mesh period for $\bar{p}_1 - \hat{p}_1$ mesh pair and 1.78 mesh period for $r - \hat{p}_1$ mesh pair, as shown in Figure 6. Such reductions occur in turn at a time interval of t_{rp}, which is 0.0358 s, and repeat at a period of $t_{\hat{p}}$, which is 0.1149 s.

The gear mesh damping coefficient c_g is set to be proportional to the mean value of the total TVMS and calculated as[17]

$$c_g = \mu_g \bar{k}_g \tag{18}$$

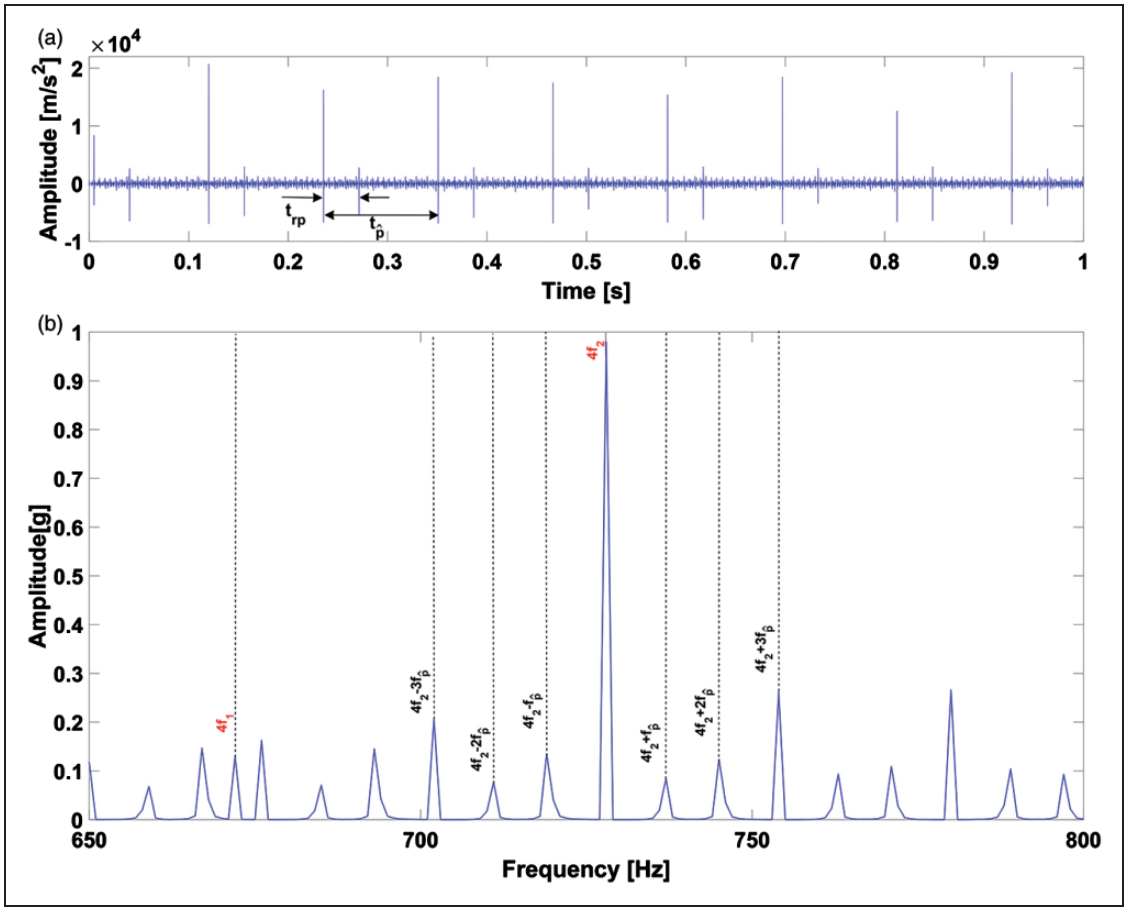

Figure 10. (a) Simulation signal and (b) zoomed-in spectrum for the gear set in the local broken planet $\hat{p}_1$ case.

Table 2. Summary of frequency components for the gear set.

	Stage 1			Stage 2				
	Sun s_1	Planet $\dot{p}_i$	Ring r	Sun s_2	Planet $\bar{p}_i$	Planet $\hat{p}_i$	Ring r	Carrier c
Rotation frequency (Hz)	0	13.6	7.9	11.7	3.1	14.3	7.9	5.6
Meshing frequency (Hz)	168			182				–
Fault characteristic frequency (Hz)	16.8	8	7	18.2	8.7	8.7	7	–

where μ_g is the scale constant measured in second. For this gear set, $\mu_{s_1\dot{p}_i} = 2.70 \times 10^{-6}$, $\mu_{r\dot{p}_i} = 3.16 \times 10^{-6}$, $\mu_{s_2\bar{p}_i} = 2.70 \times 10^{-6}$, $\mu_{r\hat{p}_i} = 3.26 \times 10^{-6}$, $\mu_{\bar{p}_i\hat{p}_i} = 2.40 \times 10^{-6}$.

To summarize, the time values are listed in Table 1. Further, the periodic changes in the TVMS will lead to corresponding vibration properties.

Simulation analysis

In this section, the simulation signals are used to demonstrate the fault properties of the planets. The motion matrix (equation (11)) are constructed and solved by using MATLAB Ode-15 s Function to obtain the dynamic responses of the gear set. During the simulation, the input speed is 700 r/min, and the load torque is 200 N.m. The acceleration signals are simulated at a sampling frequency of 5120 Hz. Other parameters are listed in Table 4 of Appendix 2. The acceleration signals in the rotational direction are extracted to illustrate the dynamic responses of the system.

The waveform and Fourier spectrum in the healthy condition are illustrated in Figure 7. The fundamental meshing frequencies are 168 Hz for the first gear stage and 182 Hz for the second gear stage, which are

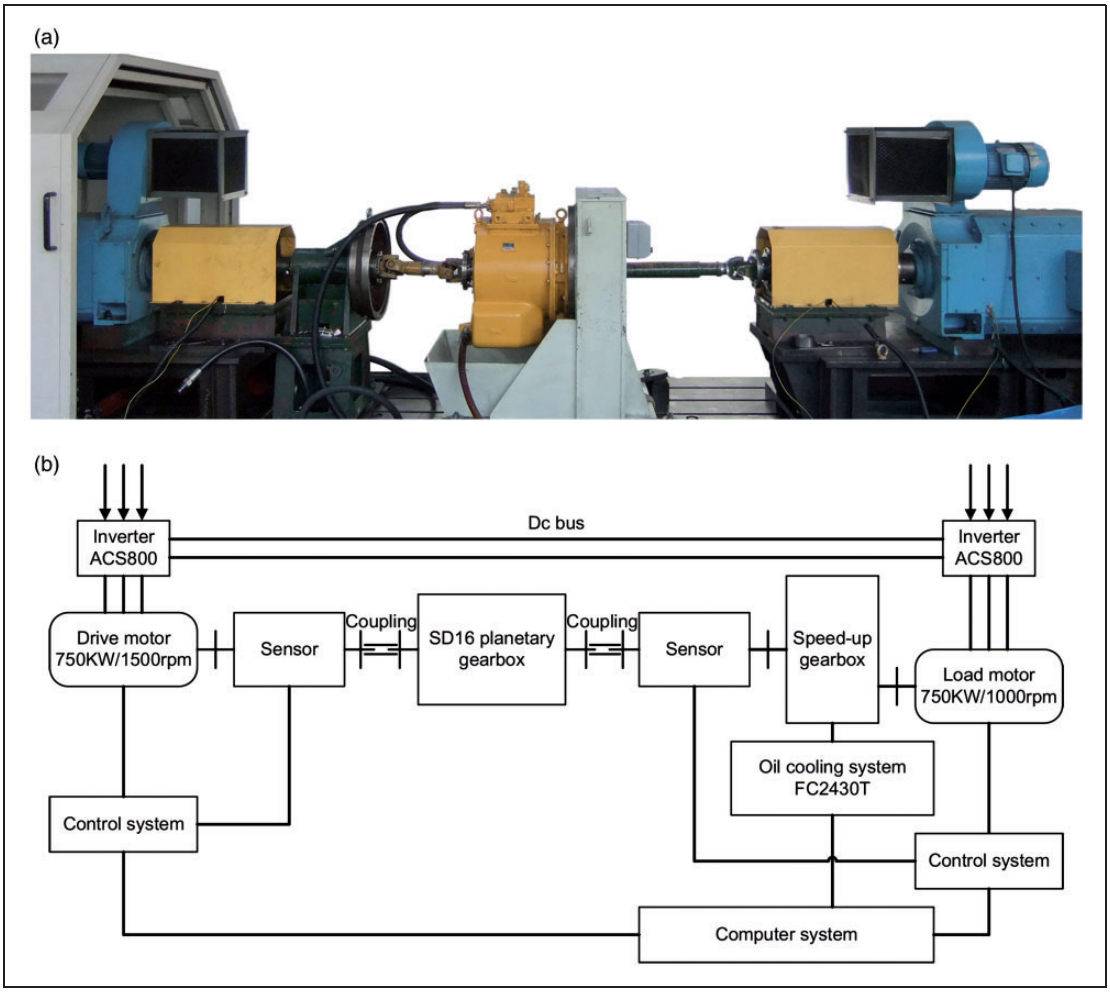

Figure 11. (a) The industrial test rig, (b) the schematic.

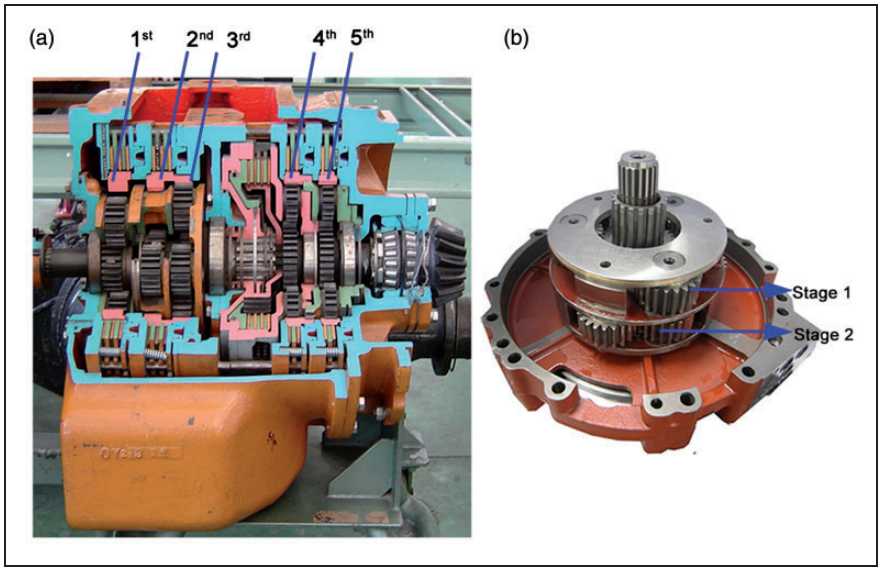

Figure 12. (a) The tested gearbox (SD16), (b) the compound gear set in the second and third gear series of the gearbox.

consistent with the mesh period of each gear stage. The harmonics kf_1 and kf_2 ($k = 1, 2, 3\ldots$) coexist in the spectrum and the kth harmonics for both gear stages are so close to each other.

Case (i): One tooth missing on $\dot{p}_1$. Figure 8(a) shows the simulation signal for the gear set in local planet $\dot{p}_1$ damage case. The first major observation is that the damaged tooth induces two close impulses in the time

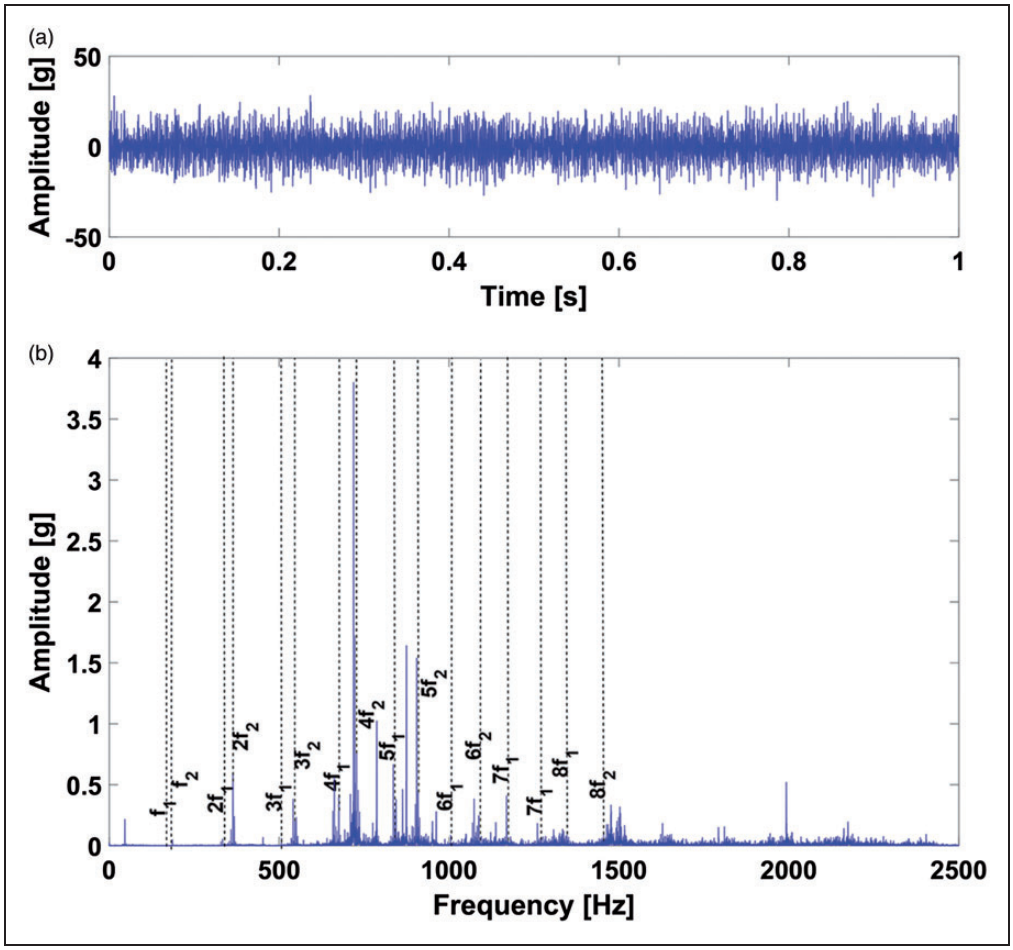

Figure 13. (a) Waveform, and (b) Fourier spectrum for the signal collected from the brand new gearbox.

domain at an interval of 0.0595 s, and such abnormal impulses occur at a period of 0.125 s. It is also noticed that the amplitudes of the impulses induced by the contact of the damaged tooth with the sun gear are bigger than those induced by the contact with the ring gear.

As a result of these impulses, the corresponding Fourier spectrum exhibits large numbers of sidebands around the kth mesh harmonic. To illustrate the details of the sideband structure, the spectrum is zoomed in around $6f_1$ and $6f_2$. As shown in Figure 8(b), all significant spectral lines of sidebands with sizable amplitudes are around $6f_1$ with a sideband spacing $f_{\dot{p}} = 8$Hz, which is the fault characteristic frequency of planet $\dot{p}_i$. It is also noted that the sidebands are asymmetric about $6f_1$. Thus, the modulation sideband frequencies in this case can be expressed as $kf_1 \pm mf_{\dot{p}} (k = 1, 2, 3\ldots, m = 1, 2, 3\ldots)$.

Case (ii): One tooth missing on $\bar{p}_1$. Figure 9(a) shows the time series for the gear set in local planet $\bar{p}_1$ damage case. Similarly, two close impulses occur in the signal, but compared with case (i), the time interval between such impulses is 0.0213 s, and these impulses occur at a period of 0.1149 s.

In the zoomed-in spectrum around $4f_1$ and $4f_2$, as presented in Figure 9(b), the fault-induced impulses produce modulation sidebands spaced at $4f_2 \pm mf_{\bar{p}}$ in an asymmetric way, where $f_{\bar{p}}$ is 8.7 Hz and is the fault characteristic frequency of planet $\bar{p}_i$. It is noticed that modulation sidebands center transfers to the kth mesh harmonic of the second gear stage when the planet in this gear stage is damaged. This phenomenon can be used to distinguish which gear stage has the damaged gear.

Case (iii): One tooth missing on $\hat{p}_1$. Finally, the time series and zoomed-in spectrum are shown in Figure 10 for local $\hat{p}_1$ damage case. Likewise, there are abnormal impulses appearing at a period of 0.1149 s in the signal, and the Fourier spectrum also exhibits rich sideband activities. It is noticed that the modulation sidebands center is still kf_2, and the fault characteristic frequency of planet $\hat{p}_i$ is also 8.7 Hz, denoted as $f_{\hat{p}}$. The main difference of the fault features in case (ii) and case (iii) is the time interval (0.0358 s) between two close fault-induced impulses, so it becomes a critical fault feature to locate the broken planet in the complex structure.

To summarize, Table 2 lists all the frequency components of this gear set.

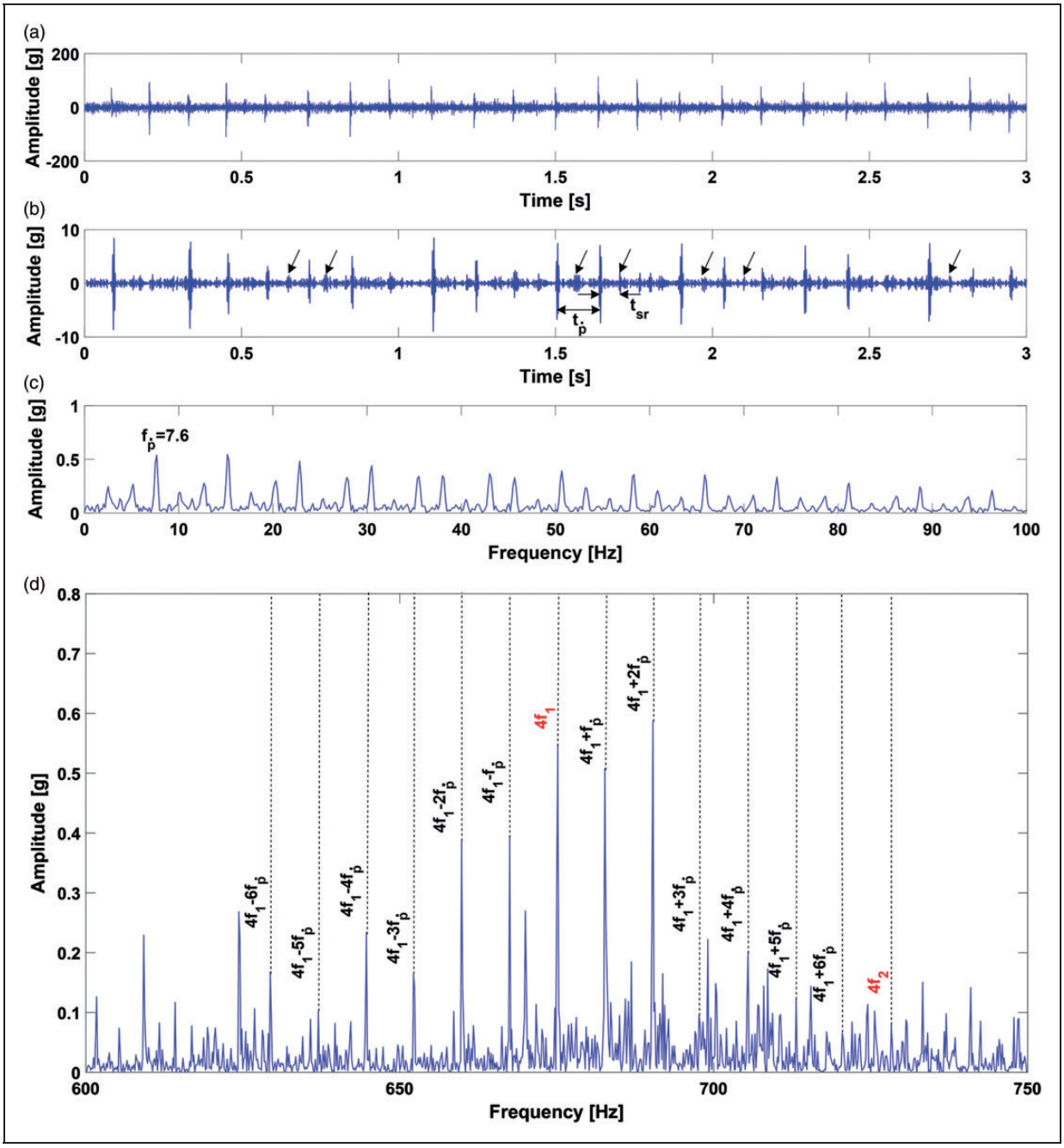

Figure 14. (a) The raw signal, (b) the filtered signal from the optimal band-pass filter, (c) the envelope spectrum of the filtered signal, and (d) the zoomed-in Fourier spectrum in case (i).

Experimental results

Experimental set-up

In this section, we analyzed several experiments conducted on an industrial site. Figure 11 shows the industrial test rig and the schematic. The tested gearboxes (SD16) are industrial gearboxes used in construction machines, which usually operate under tough working environment, such as low speed, heavy load, and muddy. Consequently, they are subject to severe damages of key components. This kind of gearboxes (see Figure 12(a)) consists of five gear series, which can provide three forward-speed and three reverse-speed ratios through activating the clutches. During the experiments, the first forward-speed ratio was implemented, in which the motor drove the input shaft at 700 r/min, and the load applied on the output shaft kept 200 N·m. This research focused on the compound gear set in the second and third gear series of the gearbox, as shown in Figure 12(b). All the parameters are the same as those in the simulation.

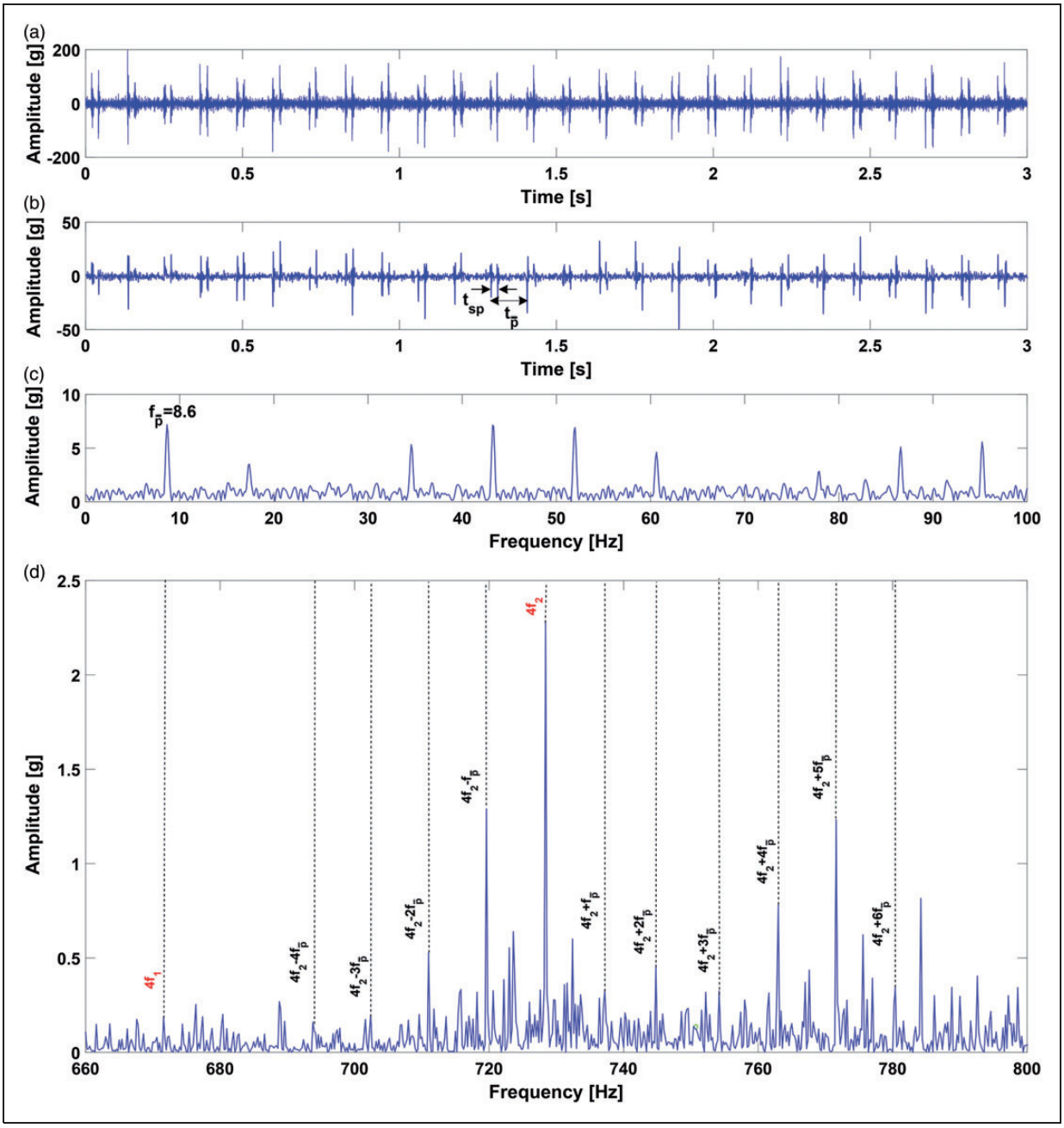

Figure 15. (a) The raw signal, (b) the filtered signal from the optimal band-pass filter, (c) the envelope spectrum of the filtered signal, and (d) the zoomed-in Fourier spectrum in case (ii).

The experiments were conducted in four steps. First, the vibration signals were acquired from a brand new gearbox as the baseline. Next, one of the planets in the first gear stage was replaced by a damaged one with a manually created damaged tooth through wire-electrode cutting. Then, the same damaged planet was used to replace one of the planets meshed with the sun gear in the second gear stage. Finally, one of the planets meshed with the ring gear in the second gear stage was replaced by the damaged one. A tri-axis accelerometer was installed on the gearbox casing to measure the vibration signals. The signal samples were measured at a sampling frequency of 5120 Hz and for a 10 min duration.

Baseline: Brand new gear box

Figure 13 shows the waveform and Fourier spectrum for the signal collected from the brand new gearbox. In the Fourier spectrum, the harmonics kf_1 and kf_2 ($k = 1, 2, 3\ldots$) coexist, where $4f_2$ is dominate, and the fundamental mesh frequencies about 168 Hz for the first stage and 182 Hz for the second stage are confirmed.

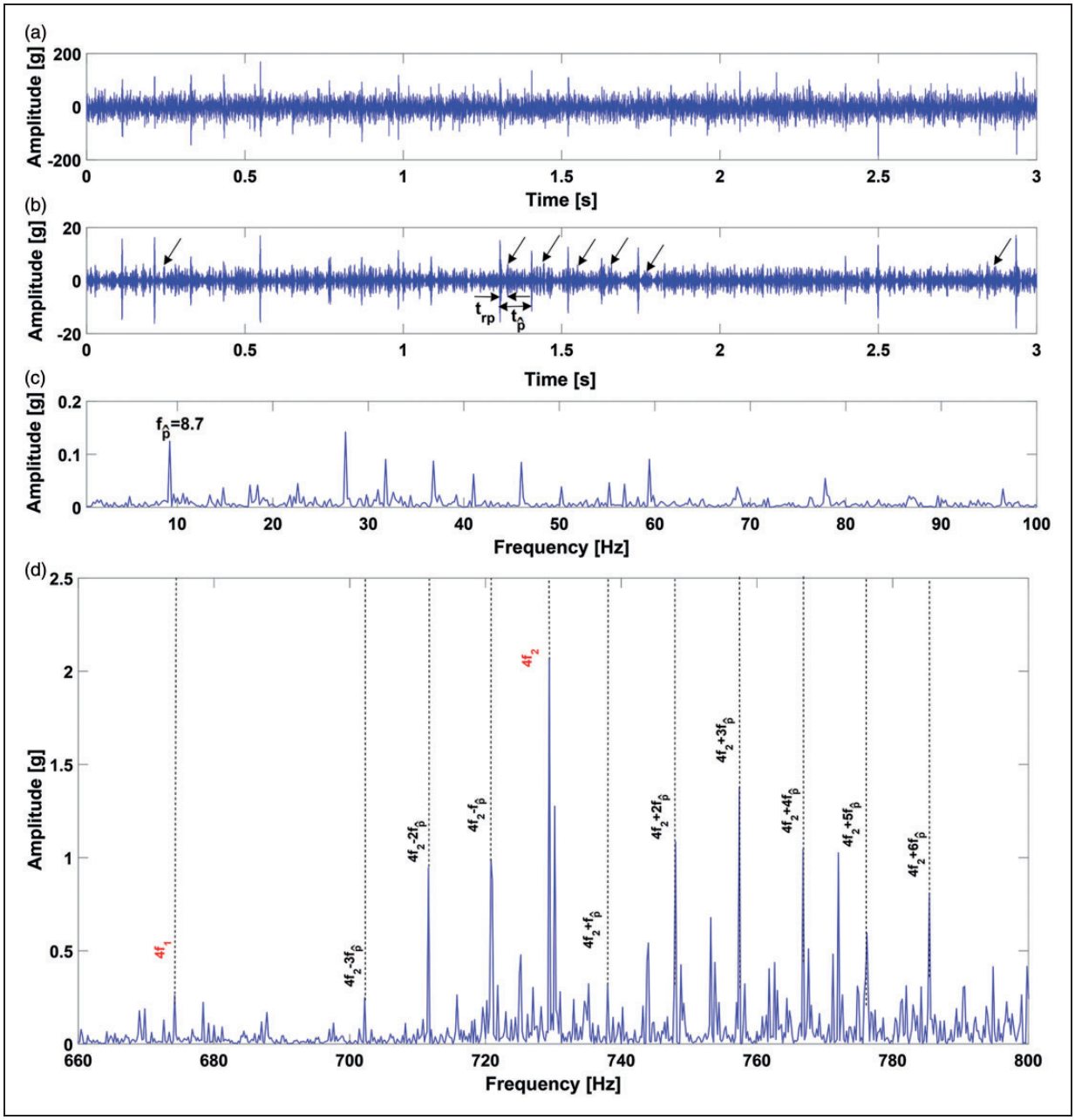

Figure 16. (a) The raw signal, (b) the filtered signal from the optimal band-pass filter, (c) the envelope spectrum of the filtered signal, and (d) the zoomed-in Fourier spectrum in case (iii).

Faulty signals analysis

Case (i): One tooth missing on $\dot{p}_i$. Figure 14(a) shows the waveform of the signal collected from the gear box with one broken planet $\dot{p}_i$. Several peaks are discovered in the raw records, which indicates that the gearbox is damaged. The intervals between these peaks are a bit varying, but a pattern of 0.13 s is found. As analyzed in the model and simulation parts, the damaged planet tooth should induce two impulses sequentially per revolution in the raw signal. However, only one impulse is visible and periodically appears in the raw signal due to the dynamic effects and external influences, as shown in Figure 14(a). In order to extract and identify the transient pattern accurately, the Spectral kurtosis method[19,20] is used to process the raw signal, and the filtered signal from the optimal band-pass filter is shown in Figure 14(b), then, two close peaks at an interval of about 0.06 s are visible, as arrowed in the figure.

Figure 14(c) presents the envelope spectrum derived based on the filtered signal. The visible peaks appear at the spectral lines of $kf_{\dot{p}}$ ($f_{\dot{p}} = 7.6$ Hz), which is consistent with the theoretical fault characteristic frequency of planet $\dot{p}_i$. In the Fourier spectrum, as presented in Figure 14(d), lots of sidebands appear around $4f_1$ with a sideband spacing equals to $f_{\dot{p}}$, and most of them have higher

amplitudes compared with the baseline signal. In general, the frequency of the mth sideband about the kth mesh harmonic is given as: $kf_1 \pm mf_{\dot{p}}$ ($k = 1, 2, 3\ldots$, $m = 1, 2, 3\ldots$).

All the features indicate the occurrence of damage on one of the planets $\dot{p}_i$, and they are consistent with our simulation analysis. Therefore, the analysis provided above validates the correctness of our model in damaged planet $\dot{p}_i$case.

Case (ii): One tooth missing on $\bar{p}_i$. Figure 15(a) and (b) shows the raw and the filtered signal collected from the gear box with one broken planet $\bar{p}_i$. Two close impulses appear in turn in the raw and filtered signal over a period of about 0.12 s, and the intervals between such two peaks fluctuate around 0.02 s.

Figure 15(c) presents the envelope spectrum derived based on the filtered signal. It is observed that the peaks appear at the spectral lines of $kf_{\bar{p}}$ ($f_{\bar{p}} = 8.6$ Hz), which is consistent with the fault characteristic frequency of planet $\bar{p}_i$. It is a normal phenomenon that the practical values fluctuate around the theoretical values due to the influence of a bit fluctuation of the input speed during the experiments.

The fault-induced impulses produce many sidebands with sizeable amplitudes in the vicinity of the mesh harmonics in the Fourier spectrum. When referring to the frequency band from 660 to 800 Hz (Figure 15(d), it further shows that most sidebands are around $4f_2$ at the frequencies $4f_2 \pm mf_{\bar{p}}$ ($m = 1, 2, 3\ldots$).

Case (iii): One tooth missing on $\hat{p}_i$. Figure 16(a) to (d) presents the raw signal, the filtered signal from the optimal band-pass filter, the envelope spectrum of the filtered signal, and the zoomed-in Fourier spectrum in this case. In the time domain, the transient impulses indicate that the gearbox is damaged, but the pattern is not clear.

In the envelope spectrum, significant peaks appear at 8.7 Hz and its multiples, which are almost the same with the frequency components presented in Figure 15(c). In the Fourier spectrum, the sidebands appear around the mesh harmonic of the second gear stage $4f_2$. Most sidebands have bigger amplitudes than the baseline signal and are located at the frequencies $4f_2 \pm 8.7m$ ($m = 1, 2, 3\ldots$). Thus, the Fourier spectral structure in this case is also similar to the results presented in Figure 15(d). According to the fault features in the spectra provided above, we can diagnose that the second gear stage has faulty planet. However, we cannot decide which group of planets are damaged.

When referring to the filtered signal, two periodic impulses are extracted. It is noticed that the time intervals between such impulses are about 0.03 s, which are consistent with the time interval of the broken planet $\hat{p}_i$ in meshing per revolution. According to this fault feature, we can finally diagnose that the fault is on planet $\hat{p}_i$. The above analysis validates the correctness of our simulation analysis in local planet $\hat{p}_i$ damage case.

Conclusions

We proposed a three-dimensional dynamic model to illustrate the fault features of the compound planetary gear set with damaged planets. In the spectra, the gear set has close meshing frequencies, the modulation sidebands appear around the mesh harmonics of the gear stage containing the faulty gear, and the sideband spacing is equal to the fault characteristic frequency of the faulty planet. However, the fault characteristic frequencies of the planets are close or even the same with each other, which make it more difficult to locate the faulty planet through spectral analysis. For such cases, we used the time interval between the two fault-induced close impulses in the time domain as an important feature to diagnose the fault. Further, we validated the theoretical derivations through experimental analysis.

Declaration of Conflicting Interests

The author(s) declared no potential conflicts of interest with respect to the research, authorship, and/or publication of this article.

Funding

The author(s) disclosed receipt of the following financial support for the research, authorship, and/or publication of this article: This research was supported by the National High Technology Research and Development Program of China (No. 2013AA040204) and the National Key Basic Research Development Plan of China (No. 2011CB013403).

References

1. McFadden PD and Smith JD. An explanation for the asymmetry of the modulation sidebands about the tooth meshing frequency in epicyclic gear vibration. *Proc IMechE, Part C: J Mechanical Engineering Science* 1985; 199: 65–70.
2. Feng Z and Zuo MJ. Vibration signal models for fault diagnosis of planetary gearboxes. *J Sound Vib* 2012; 331: 4919–4939.
3. Feng Z, Zuo MJ, Qu J, et al. Joint amplitude and frequency demodulation analysis based on local mean decomposition for fault diagnosis of planetary gearboxes. *Mech Syst Signal Process* 2013; 40: 56–75.
4. Feng Z and Zuo MJ. Fault diagnosis of planetary gearboxes via torsional vibration signal analysis. *Mech Syst Signal Process* 2013; 36: 401–421.
5. Inalpolat M and Kahraman A. A theoretical and experimental investigation of modulation sidebands of planetary gear sets. *J Sound Vib* 2009; 323: 677–696.
6. Inalpolat M and Kahraman A. A dynamic model to predict modulation sidebands of a planetary gear set having manufacturing errors. *J Sound Vib* 2010; 329: 371–393.

7. Cheng Z, Hu N and Zhang X. Crack level estimation approach for planetary gearbox based on simulation signal and GRA. *J Sound Vib* 2012; 331: 5853–5863.
8. Cheng Z and Hu N. Quantitative damage detection for planetary gear sets based on physical models. *Chin J Mech Eng* 2012; 25: 190–196.
9. Liang X, Zuo MJ and Hoseini MR. Vibration signal modeling of a planetary gear set for tooth crack detection. *Eng Fail Anal* 2015; 48: 185–200.
10. Chen Z and Shao Y. Dynamic features of a planetary gear system with tooth crack under different sizes and inclination angles. *J Vib Acoust* 2013; 135: 1–12.
11. Shao Y and Chen Z. Dynamic features of planetary gear set with tooth plastic inclination deformation due to tooth root crack. *Nonlinear Dyn* 2013; 74: 1253–1266.
12. Chen Z, Zhu Z and Shao Y. Fault feature analysis of planetary gear system with tooth root crack and flexible ring gear rim. *Eng Fail Anal* 2015; 49: 92–103.
13. Liang X, Zuo MJ and Pandey M. Analytically evaluating the influence of crack on the mesh stiffness of a planetary gear set. *Mech Mach Theory* 2014; 76: 20–38.
14. Liang X and Zuo MJ. Investigating vibration properties of a planetary gear set with a cracked tooth in a planet gear. In: *2014 annual conference of the prognostics and health management society*, Fort Worth, TX, USA, 1–8 September 2014.
15. Liang X, Zuo MJ and Liu L. A windowing and mapping strategy for gear tooth fault detection of a planetary gearbox. *Mech Syst Signal Process* 2016; 80: 445–459.
16. Liu L, Liang X and Zuo MJ. Vibration signal modeling of a planetary gear set with transmission path effect analysis. *Measurement* 2016; 85: 20–31.
17. Li G, Li F, Wang Y, et al. Fault diagnosis for a multistage planetary gear set using model-based simulation and experimental investigation. *Shock Vib* 2015; 2016: 1–19.
18. Li G, Li F, Dong D, et al. Fault status assessment for fault diagnosis of a multistage planetary gear set based on dynamic simulation and experimental analysis. In: *Sustainable design and manufacturing 2016*. Chania, ▮▮ Crete, Greece, April 2016, pp.673–686.
19. Assaad B, Eltabach M and Antoni J. Vibration based condition monitoring of a multistage epicyclic gearbox in lifting cranes. *Mech Syst Signal Process* 2014; 42: 351–367.
20. Barszcz T and Randall RB. Application of spectral kurtosis for detection of a tooth crack in the planetary gear of a wind turbine. *Mech Syst Signal Process* 2009; 23: 1352–1365.
21. Lei Y, Han D and Lin J. Planetary gearbox fault diagnosis using an adaptive stochastic resonance method. *Mech Syst Signal Process* 2013; 38: 113–124.
22. Lei Y, Liu Z, Wu X, et al. Health condition identification of multi-stage planetary gearboxes using a mRVM-based method. *Mech Syst Signal Process* 2015; 60: 289–300.
23. Lei Y, Li N, Lin J, et al. Two new features for condition monitoring and fault diagnosis of planetary gearboxes. *J Vib Control* 2013; 21: 755–764.
24. Qu J, Liu Z, Zuo M, et al. Feature selection for damage degree classification of planetary gearboxes using support vector machine. *Proc IMechE, Part C: J Mechanical Engineering Science* 2011; 225: 2250–2264.
25. Liu Z, Qu J, Zuo MJ, et al. Fault level diagnosis for planetary gearboxes using hybrid kernel feature selection and kernel Fisher discriminant analysis. *Int J Adv Manuf Technol* 2013; 67: 1217–1230.
26. Lei Y, Lin J, Zuo MJ, et al. Condition monitoring and fault diagnosis of planetary gearboxes: A review. *Measurement* 2014; 48: 292–305.
27. Kahraman A. Free torsional vibration characteristics of compound planetary gear sets. *Mech Mach Theory* 2001; 36: 953–971.
28. Inalpolat M and Kahraman A. Dynamic modelling of planetary gears of automatic transmissions. *Proc IMechE, Part K: J Multi-Body Dynamics* 2008; 222: 229–242.
29. Kiracofe DR and Parker RG. Structured vibration modes of general compound planetary gear systems. *J Vib Acoust* 2006; 129: 1–16.
30. Guo Y and Parker RG. Purely rotational model and vibration modes of compound planetary gears. *Mech Mach Theory* 2010; 45: 365–377.
31. Guo Y and Parker RG. Sensitivity of general compound planetary gear natural frequencies and vibration modes to model parameters. *J Vib Acoust* 2010; 132: 1–13.
32. Guo Y and Parker RG. Analytical determination of mesh phase relations in general compound planetary gears. *Mech Mach Theory* 2011; 46: 1869–1887.
33. Liang X, Zuo MJ and Patel TH. Evaluating the time-varying mesh stiffness of a planetary gear set using the potential energy method. *Proc IMechE, Part C: J Mechanical Engineering Science* 2013; 228: 535–547.
34. Liang X, Zhang H, Liu L, et al. The influence of tooth pitting on the mesh stiffness of a pair of external spur gears. *Mech Mach Theory* 2016; 106: 1–15.

Appendix 1

According to Liang et al.,[13,33,34] the gear tooth can be simplified as a cantilever beam on the root circle, and the improved potential energy method can be used to evaluate the TVMS. The total potential energy in a mesh pair includes four parts: Hertzian energy u_h, bending energy u_b, shear energy u_s, and axial compressive energy u_a. Based on these, the corresponding Hertzian stiffness k_h, bending stiffness k_b, shear stiffness k_s, and axial compressive stiffness k_a can be calculated.

For the single-tooth mesh duration, the total TVMS can be calculated as

$$k_g = \frac{1}{1/k_h + 1/k_{b_1} + 1/k_{s_1} + 1/k_{a_1} + 1/k_{b_2} + 1/k_{s_2} + 1/k_{a_2}} \tag{19}$$

For the double-tooth mesh duration, the total TVMS can be expressed as

$$k_g = \sum_{i=1}^{2} \times \frac{1}{1/k_{h,i} + 1/k_{b_1,i} + 1/k_{s_1,i} + 1/k_{a_1,i} + 1/k_{b_2,i} + 1/k_{s_2,i} + 1/k_{a_2,i}} \tag{20}$$

where subscripts 1 and 2 represent the driving gear and driven gear in a mesh pair, respectively. $i = 1$ represents the first mesh pair over the double-tooth mesh duration and $i = 2$ represents the second. The derivations of each stiffness component were proposed in Liang et al.[13]

For the compound planetary gear set, it comprises several sun–planet, planet–planet, and ring–planet mesh pairs. While each of the sun–planet meshes (or ring–planet meshes, planet–planet meshes) has the same shape of TVMS variation, they are not in phase with each other. Besides, there are phase differences among the sun–planet, planet–planet, and ring–planet meshes. In this study, the mesh phase relations are described by the relative phases between TVMS variation functions, which were calculated in Li et al.[17] and listed in Table 3. Incorporating the time intervals and the mesh phases, the total TVMS can be obtained.

Table 3. Relative phases of the gear set.

Stages		Relative phase									
1		γ'_{s2}	γ'_{s3}	γ'_{r1}	γ'_{r2}	γ'_{r3}	γ'_{rs}				
	0	0	0	0	0	0	0				
2	γ''_{s1}	γ''_{s2}	γ''_{s3}	γ''_{p1}	γ''_{p2}	γ''_{p3}	γ''_{r1}	γ''_{r2}	γ''_{r3}	γ''_{ps}	γ''_{rs}
	0	0	0	0	0	0	0	0	0	−0.13	+0.38

Appendix 2

Table 4. Main parameters of the gear set.

	Sun gear		Planet gear	Ring gear		Carrier
Parameters	s_1	s_2	$p_i(\dot{p}_i, \bar{p}_i, \hat{p}_i)$	r		c
Number of teeth	30	30	21	72	78	–
Module (mm)	3.5	3.5	3.5	3.5		–
Pressure angle (°)	20	20	20	20		–
Base diameter (mm)	98.668	98.668	69.067	236.803	256.536	–
Addendum diameter (mm)	112	112	80.5	245.734	266.677	–
Root diameter (mm)	96.25	96.25	64.75	260.75	281.75	
Face width (mm)	40.5	40.5	38.5	92		–
Material	20NiCrMoH	20NiCrMoH	20NiCrMoH	42CrMo		$ZG40Mn_2$
Young's modulus (Pa)	2.06×10^{11}	2.06×10^{11}	2.06×10^{11}	2.12×10^{11}		2.02×10^{11}
Poisson's ratio	0.30	0.30	0.30	0.28		0.30
Mass (kg)	2.11	2.11	0.92	11.89		15.54
Mass moment of inertia ($kg{\cdot}mm^2\times10^4$)	0.360	0.360	0.081	24.095		12.729
Transmission ratio	2.08					
Radial stiffness of the bearing (N/m)	$k_{bs_1} = k_{bs_2} = k_{bc} = k_{br} = k_{bp_i} = 10^8$					
Damping coefficient of the bearing (N·s/m)	$c_{bs_1} = c_{bs_2} = c_{bc} = c_{br} = c_{bp_i} = 10^5$					